fluids

MDPI

Article

Dynamics of a Laser-Induced Bubble above the Flat Top of a Solid Cylinder—Mushroom-Shaped Bubbles and the Fast Jet

Max Koch [1,*], Juan Manuel Rosselló [1,2], Christiane Lechner [1,3], Werner Lauterborn [1] and Robert Mettin [1,*]

[1] Drittes Physikalisches Institut, Universität Göttingen, Friedrich-Hund-Platz 1, 37077 Göttingen, Germany; jrossello.research@gmail.com (J.M.R.); christiane.lechner@tuwien.ac.at (C.L.); werner.lauterborn@phys.uni-goettingen.de (W.L.)
[2] Institut für Physik (IfP), Otto-von-Guericke-Universität Magdeburg, 39106 Magdeburg, Germany
[3] Institute of Fluid Mechanics and Heat Transfer, TU Wien, Getreidemarkt 9, 1060 Vienna, Austria
* Correspondence: max.koch@phys.uni-goettingen.de (M.K.); robert.mettin@phys.uni-goettingen.de (R.M.)

Abstract: The dynamics of a laser-induced bubble on top of a solid cylinder is studied both experimentally and numerically. When the bubble is generated close to the flat top along the axis of the cylinder and its maximum radius exceeds the one of the flat top surface, it collapses in the form of a mushroom with a footing on the cylinder, a long stem and a hat-like cap typical for a mushroom head. The head may collapse forming a thin, fast liquid jet into the stem, depending on bubble size and bubble distance to the top of the cylinder. Several experimental and numerical examples are given. The results represent a contribution to understand the behavior of bubbles collapsing close to structured surfaces and in particular, how thin, fast jets are generated.

Keywords: cavitation bubble; fast jet; multiphase flow; single bubble; laser induced cavitation; computational fluid dynamics; OpenFOAM; high-speed imaging, mushroom bubble

check for updates

Citation: Koch, M.; Rosselló, J.M.; Lechner, C.; Lauterborn, W.; Mettin, R. Dynamics of a Laser-Induced Bubble above the Flat Top of a Solid Cylinder—Mushroom-Shaped Bubbles and the Fast Jet. *Fluids* **2022**, 7, 2. https://doi.org/10.3390/fluids7010002

Academic Editors: Goodarz Ahmadi and Pouyan Talebizadeh Sardari

Received: 30 June 2021
Accepted: 8 December 2021
Published: 21 December 2021

1. Introduction

Cavitation bubbles of millimeter and sub-millimeter size have been investigated for more than 100 years. The interest arose from their destructive action on solid surfaces, notably propeller blades [1,2]. Since then it is known that cavitation possesses the ability to erode the hardest materials. However, despite considerable efforts to elucidate the erosion process by cavitation bubbles, the precise mechanisms are still under discussion. Hence, there is ongoing interest in cavitation bubble dynamics. When a cavitation bubble is formed, it usually undergoes rapid expansion and—due to ambient pressure or acoustic driving—rapid collapse with subsequent rebound and further collapses and rebounds [3,4]. The dynamics of the bubble is highly influenced by many factors: the properties of the surrounding liquid (density, viscosity), the bubble contents (gas, vapour), the bubble–liquid interface (surface tension, coating), outer factors (pressure, temperature, gravity) and, in particular, the large class of geometrical constraints, i.e., boundaries or objects nearby with different properties from flat to curved or smooth to corrugated and solid to soft. For systematic studies on geometrical constraints, isolated single bubbles are required. The liquid breakdown induced by a focused laser light pulse [5,6] has been used for this purpose. For the beginning of cavitation bubble dynamics studies with laser-seeded bubbles, see [7,8]).

Since the first studies with laser-induced bubbles in constraint geometries [7], vast knowledge has already been accumulated with this method. In particular, the phenomenon of *liquid jet formation* has been profoundly studied for different geometries, notably flat solid boundaries, but also concave and convex ones [9,10]. When the bubble expands and collapses in the vicinity of constraints, it is pierced by the liquid. The liquid parcel that flows through the bubble then is called a *jet*. Moreover, besides single spherical bubble expansion and collapse in the vicinity of an extended flat solid boundary (see, e.g., [11–16]) with its jet towards the boundary, bubble expansion and collapse in the vicinity of a free boundary (see, e.g., [17,18]) has been studied with its jet away from the boundary. Jet formation has also been studied in the vicinity of an elastic boundary (e.g., [19]) and in a (low) gravity field (see, e.g., [20–22]).

First reported experiments on jet formation started in 1961 with the work of Naudé and Ellis [23] and the availability of high-speed photography [7,20,24]. The numerical work started in 1971 with the work of Plesset and Chapman [25] and was essentially promoted by Blake and his group [11,26–29]. The solid-boundary case with its jets was and still is heavily studied (see, e.g., [13,14,16,18,30–57]). This jet is called *micro-jet* and exhibits speeds in the order of 100 m/s. The speed depends on the normalized distance D^*, that is given by

$$D^* = \frac{D_{\rm init}}{R_{\rm max,unbound}}, \tag{1}$$

where $D_{\rm init}$ is the initial distance of the (laser-induced) bubble to the solid boundary and $R_{\rm max,unbound}$ is the maximum radius the bubble would attain in an unbounded liquid. More precisely, depending on the normalized distance D^*, jet velocities between about 35 m/s at $D^* = 0.3$ and about 200 m/s at $D^* = 3$ were measured by [12,58,59] and calculated by [18,19,53,59]. A comparison of velocities of numerical simulations with experiments (with very good agreement) can be found in the work of Koch [58]. A detailed comparison of jet velocities gained by different authors and methods is given in Section 6.

Recently, it was found with the help of laser-induced bubbles that for very low initial distances of the bubble to a solid surface, a different jetting mechanism occurs, producing a *fast jet*. It was predicted numerically by Lechner et al. [60] and Pishchalnikov et al. [61] and found experimentally already by Benjamin and Ellis [20] with acoustically driven bubbles and recently by Koch et al. [59] with laser-induced bubbles. The fast jets reach speeds in the order of 1000 m/s. They are produced by annular inflow with self-impact and by squeezing the liquid into two opposite directions [62].

After finding the fast jet at an extended flat solid boundary, the question arises as to whether there exist further geometrical configurations of collapsing bubbles at boundaries or objects that provoke a fast jet as well. This is indeed the case. The configuration considered is a bubble expanding and collapsing next to the flat top of a long solid cylinder (a round pillar). Studied is the axially symmetric case, i.e., the bubble center remains on the axis of rotational symmetry of the cylinder. With an extended flat top and a small bubble, this configuration can be considered a slight variant of the extended flat solid boundary. With a shrinking flat top down to the dimensions of a bubble, deviations in the dynamics of the bubble are to be expected. Indeed, a bubble above a solid cylinder was found to have interesting dynamics—with strong association to mushroom shapes. Figure 1 shows the parameters used to characterize the case under study. It contains four independent, geometric parameters: $D_{\rm init}$—the initial distance of the laser seeded bubble to the flat top of the cylinder; $R_{\rm max,unbound}$—the maximum radius the bubble would attain after expansion in a free, unbounded liquid; $l_{\rm p}$—the length of the cylinder (height above a planar, solid boundary); $r_{\rm p}$—the radius of the cylinder. As only the case of a very long cylinder, $l_{\rm p} \gg r_{\rm p}$, is considered, the length parameter can be omitted. Thus, there is one more parameter compared to the case of the bubble close to a planar, solid boundary, which is the radius of the cylinder, $r_{\rm p}$. From these geometric parameters the dimensionless parameter D^* has already been defined. A further dimensional parameter for the size of the pillar top surface with respect to the bubble size can be defined as

$$r_{\rm p}^* = \frac{r_{\rm p}}{R_{\rm max,unbound}}, \tag{2}$$

with $r_{\rm p}^*$ the normalized radius of the flat top with respect to the maximum spherical radius in a free liquid ($R_{\rm max,unbound}$). The reference to the free bubble is chosen—rather than referencing the maximum equivalent radius of the bubble close to the cylinder, $R_{\rm max,eq}$—because the actual bubble expands to an aspherical shape with a volume, whose equivalent radius varies with D_{init} for the same initial energy (see also [49]). With the reference to $R_{\text{max,unbound}}$, the temporal normalization is uniquely defined by the Rayleigh collapse time given by

$$T_{\text{Rc}} = 0.91468 \cdot R_{\text{max,unbound}} \sqrt{\rho_\infty / p_\infty}, \tag{3}$$

where $\rho_\infty = 998.2\,\text{kg/m}^3$ and $p_\infty = 101{,}315$ Pa.

$D^* = 1$ means that the bubble with the reference definition of Equation (2) would just touch the surface, $r_p^* = 1$ means that the reference bubble in a free liquid has the same diameter as the cylindrical pillar.

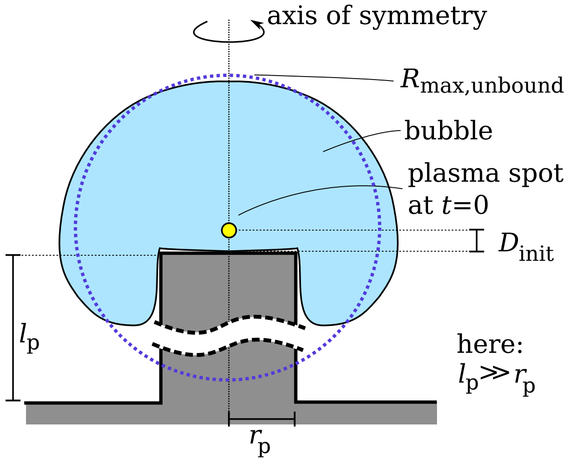

Figure 1. Sketch of the parameters for classification of bubbles close to a solid cylinder. The bubble is initiated by a hot plasma spot generated by a focused laser pulse. The radius $R_{\text{max,unbound}}$ is understood as the maximum radius of a spherical bubble with the same initial energy in an unbounded liquid. The radius of the spherical bubble with the same volume the bubble attains at maximum volume with the cylinder present (blue area) is the equivalent maximum radius $R_{\text{max,eq}}$. Note that $R_{\text{max,unbound}}$ and $R_{\text{max,eq}}$ generally have different values.

When $r_p^* \to \infty$, the limiting case of a bubble in front of a solid plane is attained. When $r_p^* \to 0$, the limiting case of a free bubble is approached. Thus the study contributes to the problem of the transition in the dynamics of a single bubble from a free bubble to a bubble restricted in its dynamics by an infinitely extended solid plane boundary. When the length of the cylinder $l_p \not\gg r_p$, l_p cannot be neglected. Then it holds for $l_p^* = l_p / R_{\text{max,unbound}} \to 0$ that the case of a bubble in front of a solid plane is approached (irrespective of r_p^*). For $l_p^* \to \infty$ the limit case studied here is obtained. The transition to pillars of small height would need substantial further work and is not studied here. The present work investigates the details of the dynamics in the parameter range $0.047 < D^* < 2.009$ and $0.251 < r_p^* < 0.893$. This parameter region covers very peculiar bubble dynamics, and, in particular, cases with experimentally observable fast-jet formation are included.

In the past, investigation of bubble dynamics near structured objects got less attention than studies on flat or smooth surfaces. However, non-flat and structured surfaces are quite relevant for various applications. Important examples include ultrasonic cleaning [63–66] and the destruction of urinary stones [61].

Oscillating bubbles in liquids are attracted to solid surfaces (see, e.g., [20], ([1], Ch. 5.9), ([30], Figure 14) and recent work [67]). Together with the fluid flow, jets and shock waves they induce upon bubble collapse, they are ideal objects to loosen and lift off contaminations from those surfaces. These properties of bubbles are widely used for cleaning purposes (see, e.g., [68–70]). Furthermore, it is known that cavitation bubbles can reach, clean and also damage crevices, holes, trenches and other complicated surface features (see, e.g., [71,72]). However, how bubbles clean or erode structured surfaces remains fundamentally unknown.

Bubble dynamics studies, as prerequisite, are therefore highly welcome. This is done in the present work for the case of a solid cylinder.

Up to now, owing to the large variety of structures and constraints, only a few cases were already investigated for single bubble dynamics. Among the solid boundaries and objects, there are a small hole [73], blind holes/crevices [74], rectangular channels [75], convex surfaces [10], a thin gap (parallel plates) [76,77], rigid spheres [78–81], a pencil-like electrode [82], ridges and grooves [83], a micro structured riblet [84], edges [85,86] and corners [87].

From the works in the above mentioned list, the work of Tomita et al. [10] and Palanker et al. [82] show mushroom shapes similar to those investigated in the present work, but the fast jets escaped their notice. None of the works on bubbles in constraint geometries of the above list report the fast jet. The maximum axial jet velocity reported in the aforementioned works amounts to 200 m/s in the case of a bubble in a thin gap, whereas in the present work velocities in the order of 1000 m/s will be presented for bubbles on top of pillars.

This work is organized as follows: The experimental methods—seeding bubbles with focused laser light and taking pictures with high-speed photography—are presented in Section 2, and the numerical methods—solving the Navier-Stokes equations with OpenFOAM—in Section 3. The experimental results are given in Section 4: Bubbles on top of the cylinder were produced and photographed according to the arrangement of Figure 2. The numerical results are presented in Section 5. The calculations were done in axial symmetry (2D) with an example in full 3D to confirm the validity of the axial-symmetry approach.

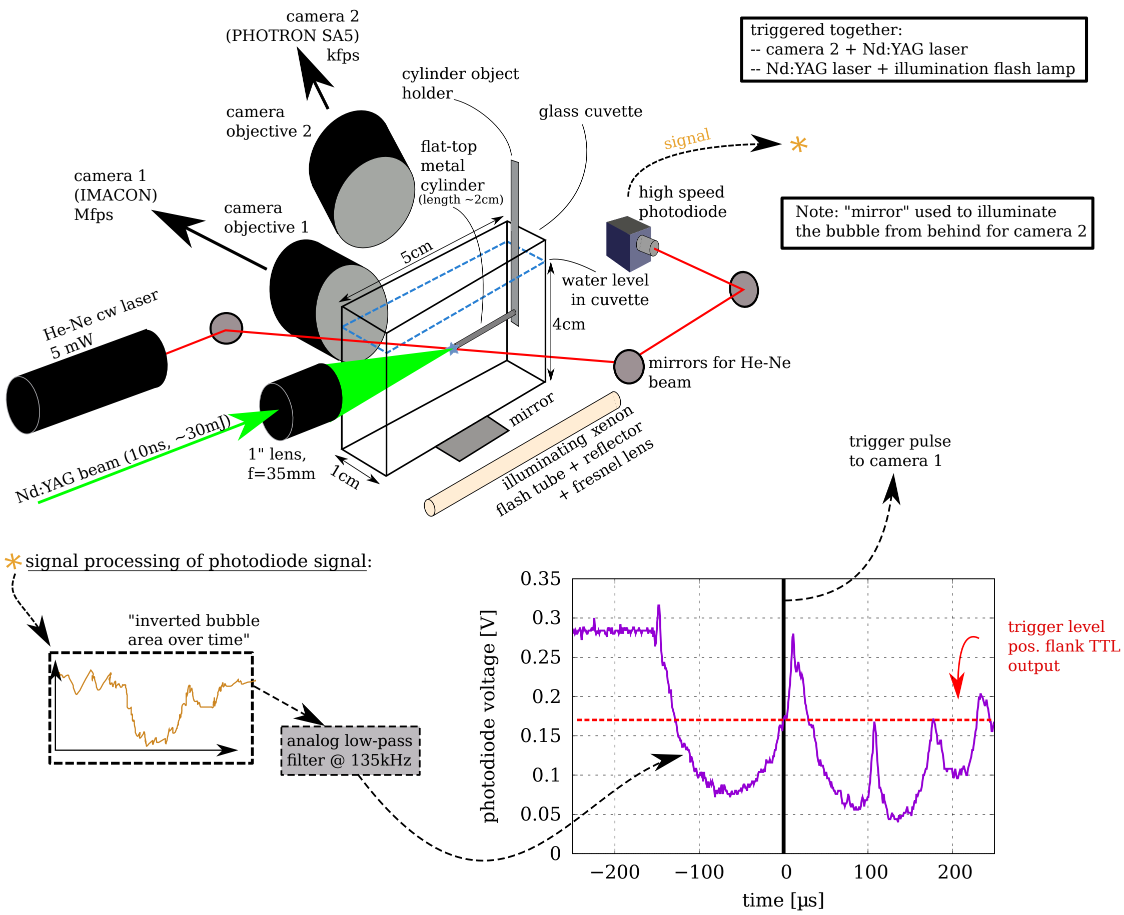

Figure 2. Sketch of the experimental arrangement. The He-Ne laser allows for triggering onto bubble dynamics phases with approximately 1 µs precision. A typical bubble "shadow" curve with trigger level is shown in the lower right inset. The xenon flash tube refers to the Mecablitz device.

2. Experimental Methods

The experimental setup is depicted in Figure 2. The design is versatile and could be used for the study of bubble dynamics at other objects as well. Here, a single bubble is generated in water by optical breakdown of a nanosecond laser pulse that is focused along the symmetry axis of the cylindrical object.

The laser pulse of wavelength 532 nm is produced by a Q-switched Nd:YAG laser (Litron Nano PIV). The laser pulse duration, $t_p = 10$ ns FWHM, was measured with a high-speed photodiode (Thorlabs SV2-FC). The impulse response of the photodiode amounts to 0.8 ns. The diode signal was recorded with a 40 Gigasamples per second ($\equiv$ 40 S/ns), 2.5 GHz (0.4 ns time resolution) bandwidth oscilloscope (Tektronix DPO 7254). The laser beam is expanded to approximately 2.5 cm in diameter and is then focused into a rectangular glass cuvette (Hellma) filled with de-ionized water at room temperature by means of a lens with a focal length of 35 mm. The laser focus-spot was placed onto the flat top of the cylinder object. The cylinder actually was a sewing pin needle, which was ground to flat-top by diamond grinding. The needle top has a diameter of (545.6 ± 5.9) µm.

The complete bubble life-time was captured with a Photron APX-RS camera (model 250 K) at a minimum shutter time of 1 µs and frame rates of 21 kiloframes per second (kfps) at 384 $\times$ 272 pixels or 100 kfps at 244 $\times$ 222 pixels. Simultaneously, pictures of the bubble evolution within a reduced time window of around 1 µs were taken with an Imacon 468 camera. This camera can record up to 100 megaframes per second (Mfps) with a sensor field of 385 $\times$ 575 pixels. However, only eight images in total are captured for any time resolution, but all eight images can be set arbitrarily in start time, exposure time and voltage gain. Both cameras were equipped with a K2 Infinity long-distance microscope with large working distances ranging from 54 mm to 200 mm. In combination with the CF-2 and CF-4 modules the K2-objectives allow for resolutions down to 4 µm/pixel (CF-2) and down to $\approx$ 2 µm/pixel (CF-4). The illumination was done from the opposite side of the imaging optics (backlighting) with the xenon flash described below. The cylinder top, i.e., the spot of bubble seeding, was put into the center of the water volume inside the glass cuvette.

To circumvent the relatively high jitter of the bubble collapse time, a trigger signal was derived from a He-Ne laser beam passing through the bubble and hitting the high-speed photodiode described above. This triggering method dates back to Lauterborn [8] and has been applied by others, too (see e.g., [88,89]). The method made it possible to capture the bubble dynamics in a repeatable manner at a desired phase, e.g., the collapse phase. The path of the He-Ne laser beam first was directed through the bubble seeding site, and then through various mirrors and pinholes onto the photodiode that was shaded against any stray light from the illumination for the recordings. Depending on the size of the bubble, the light is more or less deflected yielding a photodiode signal, which is highest when the bubble is absent. The low-pass filtered signal was fed into the oscilloscope that could generate a hardware trigger TTL output. When the photodiode voltage crossed a certain level with positive slope, this output then triggered the Imacon camera for megaframes per second (Mfps) recording. This way, the trigger accuracy could be increased to approximately 1 µs precision at the time of minimum bubble volume. This is sufficient to obtain up to 10 Mfps resolution with one single measurement to capture the bubble collapse.

To illuminate the bubbles for megaframes-per-second recordings, the optimum was reached by xenon flash tubes of minimum 30 J light emission in combination with a reflector and a Fresnel lens. The light emission duration is in the range 500 µs to 8 ms, depending on the output energy. The xenon flash used was a photo flash (Mecablitz 36CT2) with a straight flash tube of 35 mm length and about 35 J output, directed onto a Fresnel lens. The amount of light reaching each of the camera objectives had to be adapted according to their specific shutter speeds. This was done by reflecting only part of the light from the flash beam towards the objective of the Photron camera.

3. Numerical Methods

An extended description of the numerical method is given in Koch et al. [42], Lechner et al. [53] and Koch [58]. For the convenience of the reader, the essential details are repeated here with respect to the special situation of the present study, for instance the grid settings.

3.1. Bubble Model

A bubble model for a cold liquid (a liquid far from its boiling point, (cf. [1])) with the following properties is used. The bubble contains a small amount of non-condensable gas to comply with experiments [42,90–92]. The vapor pressure is small compared to the ambient pressure and is neglected. The phenomenon of laser-induced breakdown to produce a bubble is not modelled. Instead, an initial bubble of high internal pressure is taken that expands to the experimental maximum radius. The condensation of the vapour part in the bubble is modelled by a reduction of the radius at rest of the bubble, R_n. More details are given below and in Appendix A. The validity of the approach has been checked by comparison with experiments in a similar approach [42] and is further demonstrated in Figure A1 in Appendix A. The liquid is taken as compressible for inclusion of pressure waves up to weak shock waves [42]. Thermodynamic effects and mass exchange through the bubble wall are neglected. Gravity can be omitted due to the small size of the bubble. Surface tension does not play a significant role for the phenomena described here and, therefore, is not included, see the discussion in Ref. [53].

3.2. Equations of Motion

The equations of motion of the two-phase flow are formulated in the "one-fluid" approach, i.e., with one density field $\rho(\boldsymbol{x},t)$, one velocity field $\boldsymbol{U}(\boldsymbol{x},t)$, and one pressure field $p(\boldsymbol{x},t)$, satisfying the Navier-Stokes Equation (4) and the continuity Equation (5):

$$\frac{\partial(\rho\boldsymbol{U})}{\partial t} + \boldsymbol{\nabla}\cdot(\rho\boldsymbol{U}\otimes\boldsymbol{U}) = -\boldsymbol{\nabla}p + \boldsymbol{\nabla}\cdot\left[\mu\left(\boldsymbol{\nabla}\boldsymbol{U} + (\boldsymbol{\nabla}\boldsymbol{U})^T - \frac{2}{3}(\boldsymbol{\nabla}\cdot\boldsymbol{U})\,\mathbb{I}\right)\right], \tag{4}$$

$$\frac{\partial\rho}{\partial t} + \boldsymbol{\nabla}\cdot(\rho\boldsymbol{U}) = 0\,. \tag{5}$$

$\boldsymbol{\nabla}$ denotes the gradient, $\boldsymbol{\nabla}\cdot$ is the divergence, and $\otimes$ the tensorial product. $\mu(\boldsymbol{x},t)$ denotes the viscosity field and $\mathbb{I}$ the unit tensor. Viscosity is included as it was found essential for the dynamics of a bubble close to a solid boundary [53,60].

In order to distinguish between liquid (l) and gas (g), volume fraction fields $\alpha_l(\boldsymbol{x},t)$ and $\alpha_g(\boldsymbol{x},t)$ are introduced with $\alpha_l = 1$ in the liquid phase, $\alpha_l = 0$ in the gas phase, and $\alpha_g(\boldsymbol{x},t) = 1 - \alpha_l(\boldsymbol{x},t)$. The position of the interface is then given implicitly by the transition of α_l from 1 to 0. The viscosity field $\mu(\boldsymbol{x},t)$ can be written as $\mu(\boldsymbol{x},t) = \alpha_l(\boldsymbol{x},t)\mu_l + \alpha_g(\boldsymbol{x},t)\mu_g$ (see, e.g., [93]). The dynamic viscosities μ_l of the liquid and μ_g of the gas are taken to be constant ($\mu_l = 1.002\times10^{-3}\,\mathrm{kg\,s^{-1}\,m^{-1}}$, $\mu_g = 1.86\times10^{-5}\,\mathrm{kg\,s^{-1}\,m^{-1}}$). The density field $\rho(\boldsymbol{x},t)$ is given by $\rho(\boldsymbol{x},t) = \alpha_l(\boldsymbol{x},t)\rho_l(\boldsymbol{x},t) + \alpha_g(\boldsymbol{x},t)\rho_g(\boldsymbol{x},t)$ with ρ_l and ρ_g the densities of the liquid and gas, respectively. As there is no mass transfer between bubble interior (gas) and exterior (liquid), the respective phase-fraction density fields $\alpha_l\rho_l$ and $\alpha_g\rho_g$ separately obey the continuity equation

$$\frac{\partial(\alpha_i\rho_i)}{\partial t} + \boldsymbol{\nabla}\cdot(\alpha_i\rho_i\boldsymbol{U}) = 0\,, \qquad i = l,g\,. \tag{6}$$

The equations of motion are closed by the equations of state for the gas and the liquid. For the gas in the bubble, the change of state is assumed to be adiabatic,

$$\rho_g(p) = \rho_{gn}(p/p_n)^{1/\gamma_g}, \tag{7}$$

with p_n and ρ_{gn} the pressure and the density of the gas in the bubble of equilibrium radius R_n at normal conditions, respectively, and $\gamma_g = 1.4$ the ratio of the specific heats of the gas (air). For the liquid, the Tait equation of state for water is used (see, e.g., [90]):

$$\rho_l(p) = \rho_\infty((p+B)/(p_\infty + B))^{1/n_T} \tag{8}$$

with p_∞ the atmospheric pressure, ρ_∞ the equilibrium density, the Tait exponent $n_\mathrm{T} = 7.15$ and the Tait pressure $B = 305$ MPa.

The segregated, pressure-based two-phase solver `compressibleInterFoam` of the open source package OpenFOAM is used for the implementation of the equations. For details, see the description and validation in Refs. [42,53,59]. Discretization of the above partial differential equations is done with the finite volume method. Because of the segregated nature of the solver, the phase with lower density (gas) undergoes a mass conservation error over time, if not accurately compensated. This was noted already in [42,94]. In the present case, the solver was altered in such a way that the continuity Equation (6) for the gas phase is re-evaluated right after the last iteration over the pressure equation. Details about this procedure are given in Appendix B.

3.3. Initial and Boundary Conditions, Meshes, and Time Steps

Initially, a spherical bubble with high internal pressure is placed at a distance D_init from the top of the cylinder in a still liquid under ambient pressure p_∞. The initial bubble radius is set to $R_\mathrm{init} = 20$ µm for all simulations. The bubble gas content is defined by the equilibrium radius R_n, when mass exchange across the interface is neglected, as in the present model. In reality, rapid evaporation, condensation and gas diffusion phenomena may play a role at the bubble interface. A simple approximation was chosen to account for it. In [95], a good agreement between simulations with the Gilmore model of a spherical bubble and experiments could be achieved by reducing the equilibrium bubble radius R_n by 60% during each local maximum of the bubble radius. In order to model both the strong first expansion and strong collapse of the bubble, a very high initial gas content, hence high $R_{n,1}$, is chosen that is linearly reduced in a specified time interval to approximately one third, hence $R_{n,2}$. Details on this procedure are given in Appendix A. The initial pressure in the bubble is obtained by compressing the gas content in the bubble adiabatically from the equilibrium radius $R_{n,1}$ to R_init, i.e., $p_{g,\mathrm{init}} = p_n(R_{n,1}^3/R_\mathrm{init}^3)^{\gamma_g}$, resulting in values of a few GPa for the cases studied here. Details on how the initial data are set are given in Appendix C. For a fixed $R_\mathrm{init} = 20$ µm the following equation describes the relation between the initial data ($R_{n,1}$) and the resulting $R_\mathrm{max,unbound}$:

$$R_\mathrm{max,unbound}\,[\mu\mathrm{m}] = 3.1662 \cdot R_{n,1}\,[\mu\mathrm{m}] - 83.1\,[\mu\mathrm{m}]. \tag{9}$$

The Equation (9) is found for $R_n \in [97\,\mu\mathrm{m}, 227.25\,\mu\mathrm{m}]$. When including larger values of R_n the relation becomes slightly non-linear. Simulations were mainly carried out in axial symmetry ("2D"). Distinct simulations were performed in full 3D. A sketch of the numerical set-up together with the grid parameters of the meshes is given in Figure 3. The mesh consists of a symmetry axis on the y-axis, as well as a central region, $x, |y| < \mathrm{Xi} = 80\,\mu\mathrm{m}$, with Cartesian orientation of cells and uniform grid spacing $\Delta x = 1\,\mu\mathrm{m}$ and $\Delta y = 1\,\mu\mathrm{m}$. Via a transition region between Xi and Xii, the Cartesian grid is matched to a polar grid. The polar grid starts from $r = \sqrt{x^2 + y^2} = \mathrm{Xii} \approx 136\,\mu\mathrm{m}$. Cells in the polar grid have an aspect ratio of unity up to a distance of $r = \mathrm{X} \approx 1.04$ mm. Further out, a stronger radial edge grading $g_f \approx 5$ of the cells is applied, so that the cells become longer in the radial direction. This numerically dampens outgoing shock waves, while keeping the overall cell amount low. The outer boundary of the computational domain is located at a distance of 52 mm from the origin. The utility `snappyHexMesh` is used to remove the cylinder with radius r_p from the mesh in the region $\{x \in \{0, r_\mathrm{p}\},\ y \in \{-52\,\mathrm{mm}, -D_\mathrm{init}\}\}$. The 2D mesh consists of 106,827 cells.

The 3D mesh (see Figure 3, right) consists of 5.2 M cells. The domain is a simple cubical box of 10 mm edge length discretized with Cartesian grid cells. The cylinder with its flat top in the center of the cube is cut out of the mesh again with `snappyHexMesh`. The base mesh consists of 46 × 46 × 46 cells with uniform grid spacing. Towards the inner center the cells are refined in domains of concentric spheres such that a final cell edge length of 1.7 µm is achieved, see Figure 3 (right) for a sketch. The innermost refinement domain has a radius of 65 µm and is centered around the origin of the initial bubble. The limited cube domain size of 10 mm edge length clearly lowers the maximum extension of the bubble, therefore the results of the 3D calculations shown here are meant to be understood in a qualitative way. They were done to show the validity of the 2D approach.

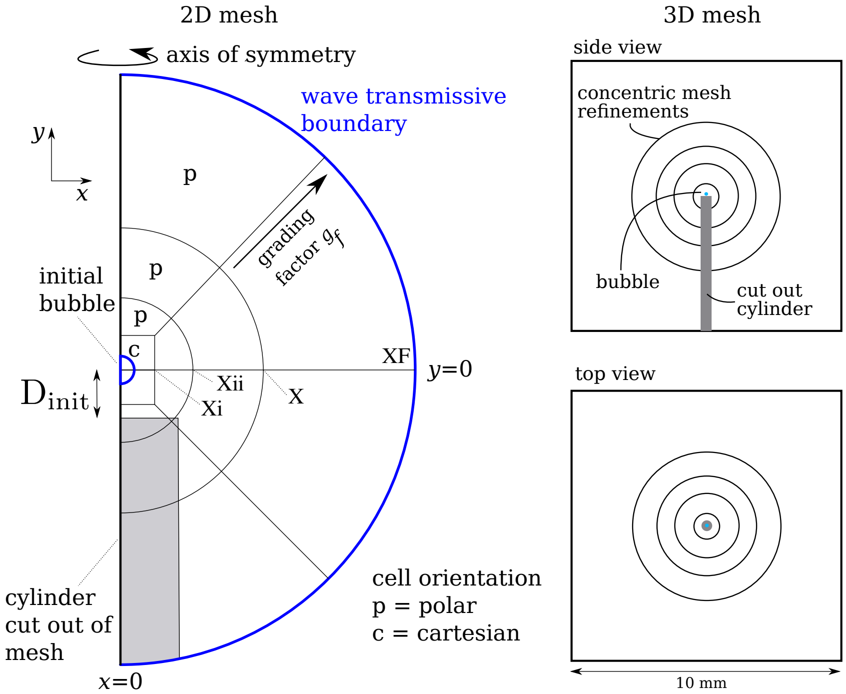

Figure 3. Sketch of the numerical set-up (not to scale) and grid parameters of the 2D mesh (**left**) and sketch of the computational domain and refinement regions for the Cartesian 3D mesh (**right**). The 2D mesh consists of 106 827 cells. The Cartesian 3D mesh consists of 5.2 million cells.

The boundary condition for the outer boundary is set to be `wave transmissive` with a maintenance of an average pressure of p_∞ =101,315 Pa. At the surface of the cylinder a no-slip condition for the velocity and zero-gradient condition for pressure is imposed. In addition, $\alpha_l = 1$ to account for a liquid layer without the need to precisely resolve it.

The *Courant number* of the flow, Co, is calculated to determine the time step size Δt for adaptive time stepping. Moreover, the Courant number of the interface, $\mathrm{Co_i}$, and the acoustical Courant number, $\mathrm{Co_a}$, are introduced in a similar manner:

$$\mathrm{Co}(\mathbf{x}) = \frac{\Delta t}{\Delta x(\mathbf{x})} \cdot |\mathbf{U}|(\mathbf{x}), \quad \mathrm{Co_i}(\mathbf{x}) = \frac{\Delta t}{\Delta x(\mathbf{x})} \cdot |\mathbf{nU}|(\mathbf{x}), \quad \mathrm{Co_a}(\mathbf{x}) = \frac{\Delta t}{\Delta x(\mathbf{x})} \cdot (c + |\mathbf{U}|)(\mathbf{x}), \tag{10}$$

with $\mathbf{n}$ the normal vector on the interface and $c(\mathbf{x})$ the local speed of sound. The time-step criterion is set such that the maximum flow Courant number, Co, and interface Courant number, $\mathrm{Co_i}$, should stay below 0.2 and the maximum acoustic Courant number, $\mathrm{Co_a}$, should be below 1 during periods of bubble evolution, where compressibility effects are important [42].

3.4. Validation

The code has been validated extensively by comparison with ordinary differential equation models for bubble collapse in spherical symmetry (the Gilmore model) in [42] and by comparison with experimental data also in axial symmetry and full 3D for the asymmetric collapse of a bubble close to a flat solid boundary in [42,53,58,59]. All these comparisons demonstrate excellent agreement for the evolution of the bubble shape between the experiments and the numerical simulation. A further example of a visual comparison for a bubble next to a flat solid boundary is given in Appendix A. The jet velocities versus D^* found by different authors via simulation and measurements are given in Section 6. The jet velocities gained by the present code are compared to measurements and to values of the simulations of totally different codes with excellent agreement. A comparison of the bubble shape between experiment and numerical simulation for a bubble close to the top of a cylinder, as investigated here, is given in Section 5.1.

4. Experimental Results

The typical mushroom-bubble dynamics with its special collapse and rebound on top of a long pillar is presented in the following. Usually, two to five ultra-high-speed Imacon measurements of the bubble collapse phase were taken for concatenating the short sequences. They were complemented with the respective photodiode signals (see Figure 2) and lower-speed Photron recordings for an overview of the bubble dynamics from bubble generation to rebound. The time from bubble generation to collapse is about 160 µs for the bubble studied.

4.1. Typical Mushroom Bubble Dynamics

As an introduction to the dynamics of a bubble on top of a rigid cylinder, the image sequence in Figure 4 is given. It depicts a stacking/interleaving of four measurements from the Photron APX-RS camera view, each recorded at 21,000 fps with a resolution of 384 $\times$ 272 pixels. By interleaving repeated recordings of bubbles of the same size, an approximate time resolution of 84 kfps is obtained.

The main aspects of the mushroom-bubble dynamics are visible in Figure 4. At first, the bubble is overlapping and embracing the cylinder edge during expansion. During collapse, a neck is formed, together with the mushroom's head. The final bubble collapse and the rebound turn the mushroom shape into a blurred one, but the neck seems to persist for a longer time during rebound. In the rebound phase, the collapsed former mushroom head expands and gets quite large, but stays smaller than the expanded bubble before. Finally, it detaches from the cylinder like a projectile. When viewing the raw video of one of the experiments, a shaking of the needle in axial direction due to the momentum transfer can be observed after the bubble is gone.

4.2. Typical Mushroom-Bubble Collapse and Rebound

The ultra-high-speed Imacon camera recording shown in Figure 5 (corresponding to the measurement presented in Figure 4) allows for a more detailed insight into the dynamics of the peculiar mushroom collapse and rebound phase.

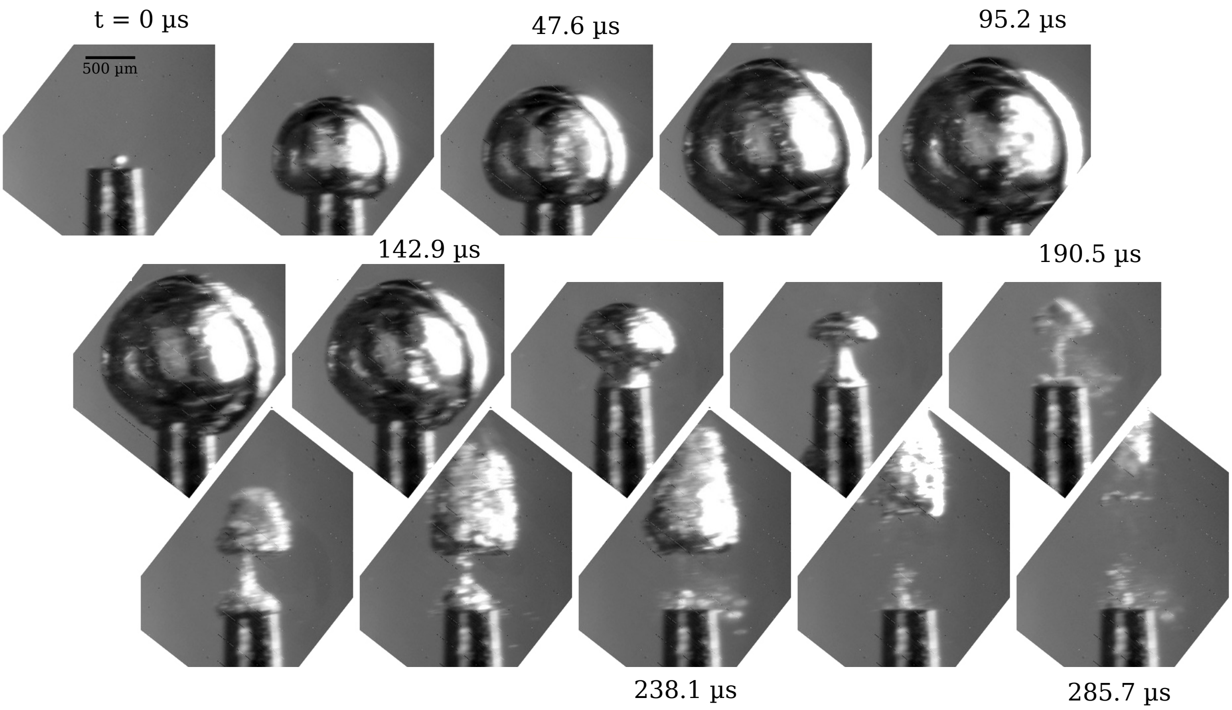

Figure 4. Image sequence of a typical mushroom bubble generated in the center of the top surface of a metal cylinder at $D^* \approx 0$. Radius of the cylinder top is $r_\mathrm{p} = 272.8\,\mu\mathrm{m}$. Exposure time is 1 µs. Stacked and interleaved sequences of four recordings with the Photron camera at 21 kfps each. The times for one of the sequences are given. The frames without a time tag are taken from different measurements as an interpolation. The bubble has a maximum horizontal width of 1689 µm ± 18 µm at 95.2 µs.

These images were taken at frame rates of 317 kfps and 870 kfps. The exposure time was 150 ns and the sequence starts from shortly after maximum bubble volume. The observer may expect a violent neck closure in the middle of the neck in frame 7, where it is narrowest. However, this neck closure will not happen. Even more astonishing is the apparent, perfectly straight cylindrical neck in frame 8 and the mushroom cap, thin and transparent like a jellyfish. In the early rebound phase in frame 10, secondary cavitation leads to tiny bubbles around the neck, reminding of the mushroom annulus in real mushrooms. Afterwards, the mushroom's head expands further and turns into a cloudy projectile, not reported on the time scale of Figure 5, but seen in the last frames of Figure 4.

In Figure 6, five frames of five prominent measurements are put together to show the moment of collapse. In view of the repeatability of the measurements, it seems that the bulk gas "under the cap" of the mushroom cap shrinks to the top below the cap while the stem homogeneously becomes more tapered on the full length. The terminology convention for the different parts of the bubble is given in Figure 7.

To obtain more insight into the very moment before and after each frame in Figure 6, a closer look into the stem dynamics at higher time resolution is needed. In Figure 8, the sequences of further experiments are stacked to elucidate the dynamics of neck formation and its subsequent evolution. The exposure time has been reduced to 30 ns and a recording speed of 10 Mfps was applied. It is observed that between frame 4 and 5 of Figure 8 the neck closure is expected to happen but it just stays stable for several frames and develops into a long gas cylinder reminding of a mushroom stem. Actually, in the further frames, the lower part of the stem recedes to form a "bottom stand foot". Its peak seems to slide down the stem. The bottom stand foot further decreases its height, while the mushroom stem collapses first in the upper half, subsequently in the lower half. The bottom stand foot has not reached zero height yet, when the mushroom stem is already expanding again as an irregular line of small bubbles in their rebound phases.

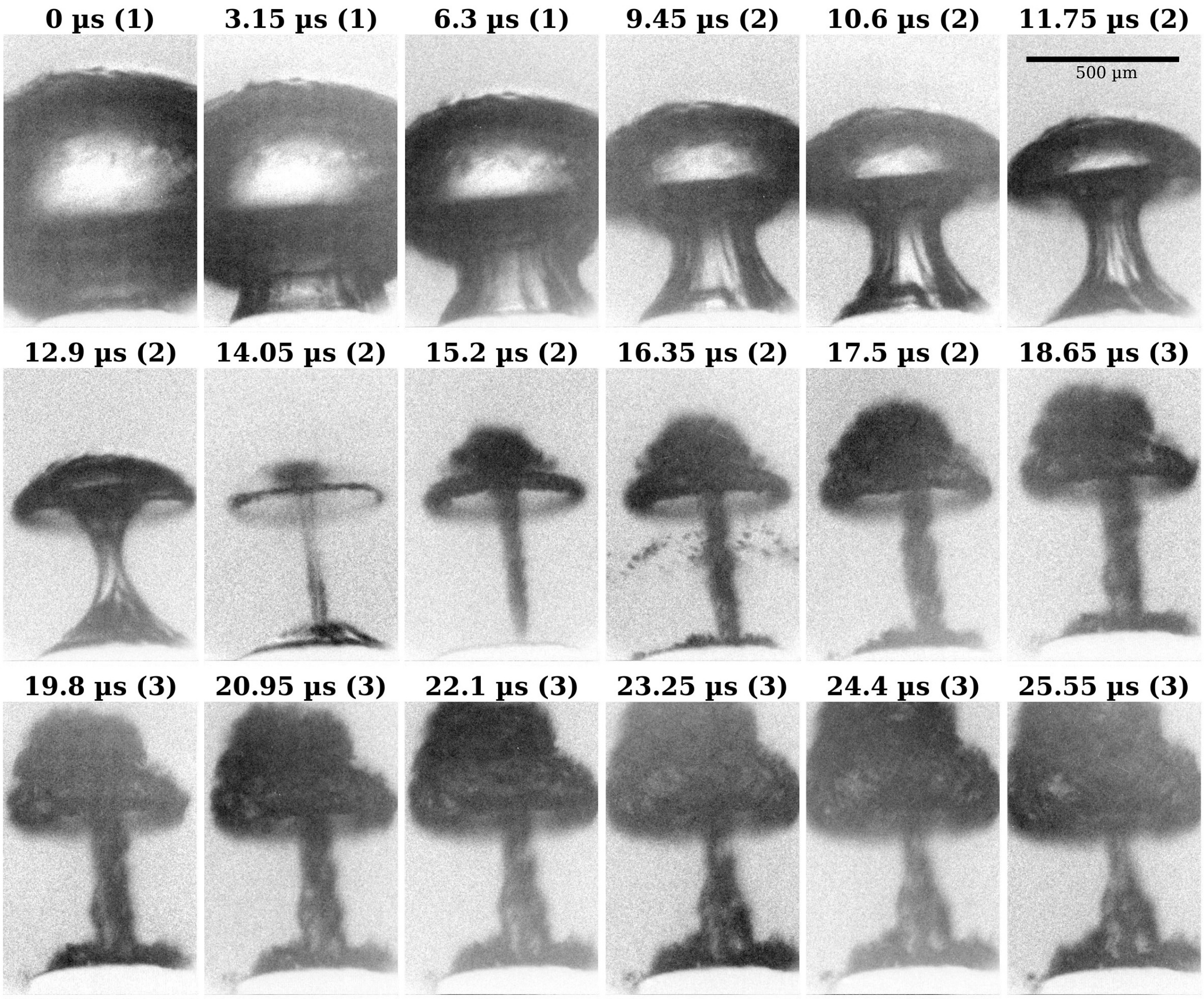

Figure 5. Experimental images of a mushroom bubble at $D^* \approx 0$ similar to Figure 4, but recorded with the substantially higher frame rate of the IMACON camera. Exposure time is 150 ns. Sequences of three recordings are stacked together. The respective recording numbers are denoted in parentheses. Frame rates for the sequences are: (1) 317 kfps and for (2) and (3) 870 kfps. Background of the images was subtracted; then the space occupied by the needle is shown in white pixels. Frame width is 633.5 µm ± 6.9 µm.

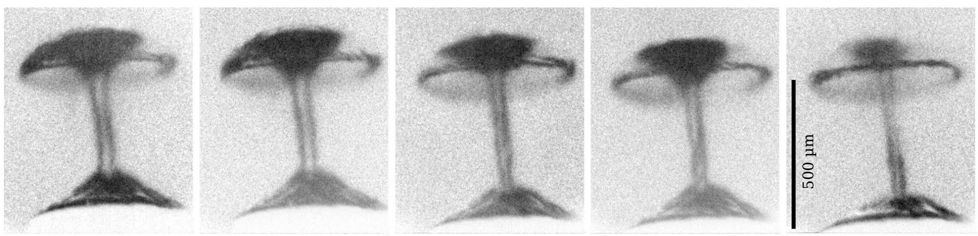

Figure 6. Repeatability of the experiments. Five experimental images from five different recordings of mushroom bubbles at $D^* \approx 0$ similar to Figure 5, extracted at time instants, where the mushroom shape is thinnest. Background of the images was subtracted. Frame width is 633.5 µm ± 6.9 µm.

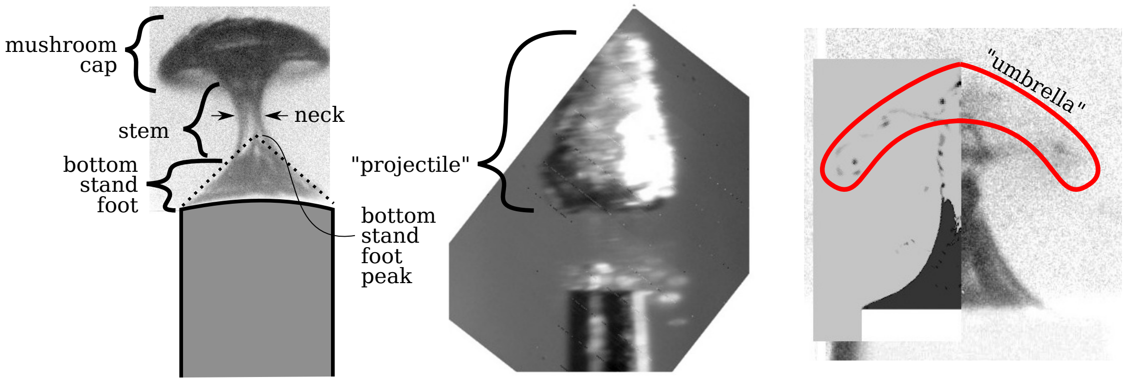

Figure 7. Terminology for mushroom-shaped bubbles.

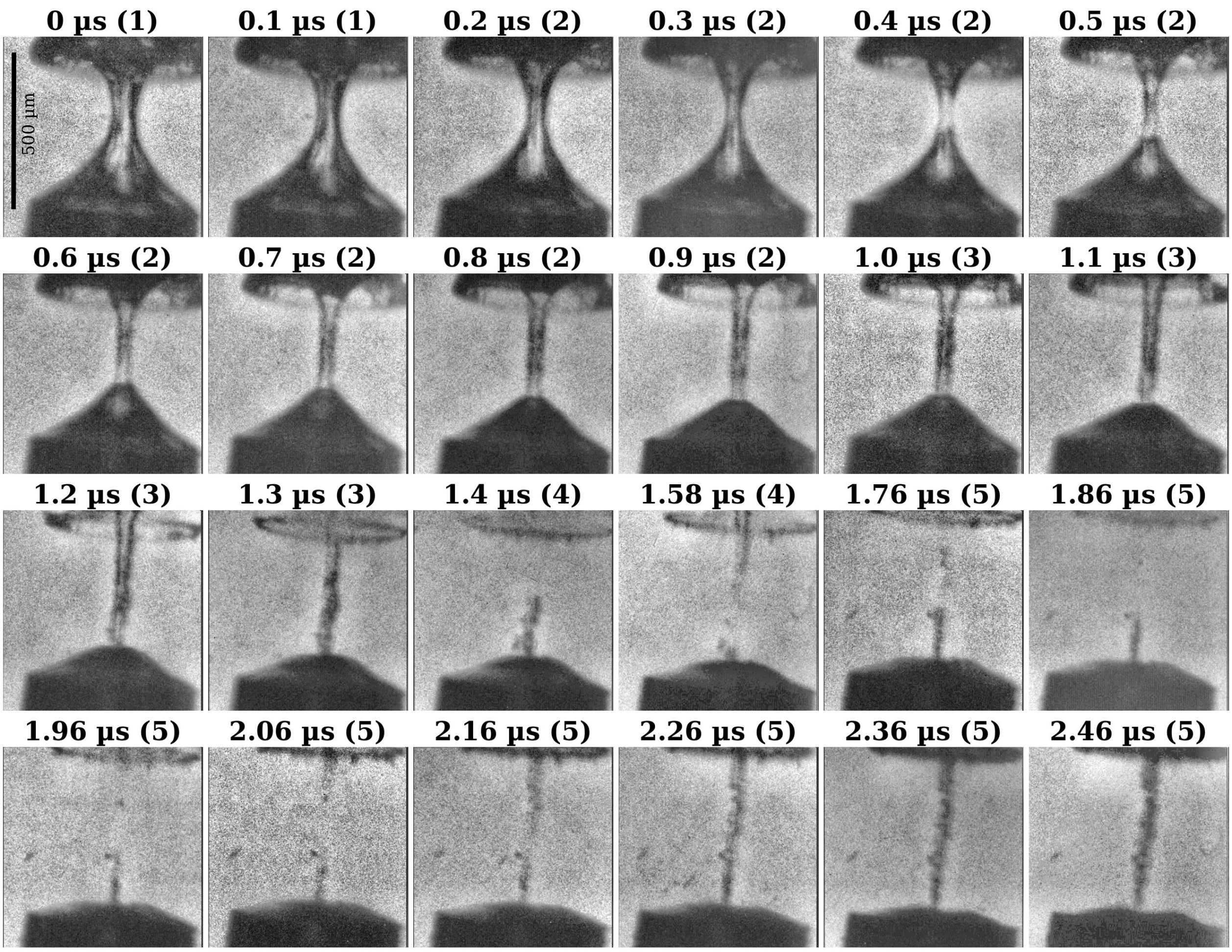

Figure 8. Neck and stem dynamics of a mushroom-shaped bubble for $D^* \approx 0$, $r_p = 272.8\,\mu\text{m}$. Experimental images of a bubble similar to Figures 4 and 5, but with ultra-high-speed frame rate (10,000,000 fps and 5,555,556 fps). Exposure time is 30 ns. Five recordings are stacked together (recording number in parentheses). Frame width is 633.5 µm ± 6.9 µm.

5. Numerical Results

The CFD simulations were performed in axial symmetry (89 cases studied) and, for a distinct case, in full 3D to show the validity of the axial-symmetry approach. For all cases, the surface tension was neglected. The radii r_{p} of the cylinder were set to 200 µm and 160 µm. In the following sections the simulations are related to the experimental results, afterwards the general dynamics of the mushroom-shape formation are presented and lastly the set of 89 cases is evaluated.

5.1. Comparison of an Experimental Mushroom Bubble with Simulations

The code was tested for its validity in several studies on bubble dynamics by comparison with experiments [42,53,59]. Here, a further comparison, now with an experimental mushroom-shaped bubble, is given for the convenience of the reader to trust the results.

In Figure 9, eight frames from an Imacon recording of are compared to a simulation in axial symmetry with matching set of r_{p}^* and D^*. Shown is the moment of self-impact of the annular inflow at the top of the mushroom cap. The experiments show a pronounced brim of the hat-like gaseous structure, the "umbrella". The simulations confirm the brim by a remainder bubble at the end of the chain of isolated, sub-resolution bubbles that form the umbrella. Note that the bubbles of the umbrella in the simulation images are ring shaped as well due to axial symmetry. Sub-resolution here means that the cells in question are filled only to a slight extent with gas, resulting in $\alpha_l \to 1$ but not $\alpha_l = 1$. This is also seen in the experimental case as a transparent, grey cap, presumably consisting of many tiny bubbles. A very good agreement of the simulation with the experiment can be stated.

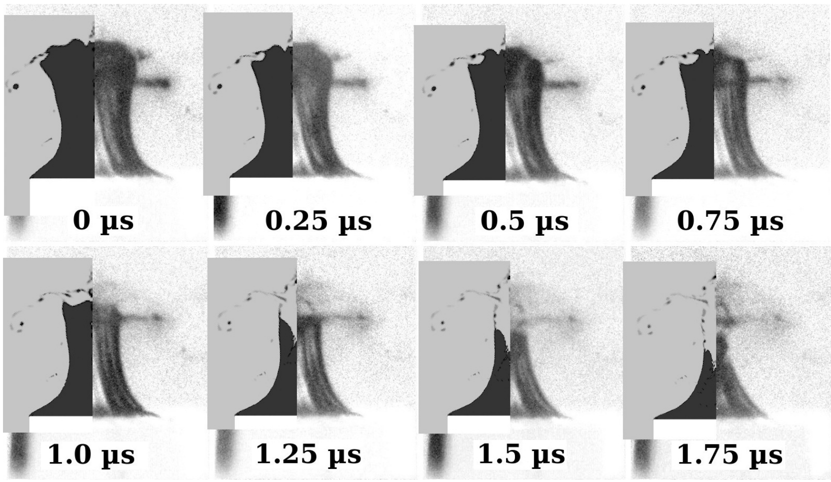

Figure 9. Imacon camera frame sequence of a mushroom bubble at a time during ring jet impact at the top of the mushroom cap. Times denote the delay to the camera trigger. Overlay with the volume fraction field α_l from the axisymmetric, numerical simulation of a bubble at $D^* = 0.057$ and $r_{\mathrm{p}}^* = 0.306$ (mind that the numerical simulation is represented by a cut through the bubble). Background of the experimental images was subtracted. Frame width is 766 µm ± 10 µm. The cylinder radius r_{p} in the experiment is 272.8 µm, in the simulation r_{p} is 200 µm.

5.2. Pressure, Velocity and Flow Fields of a Mushroom Bubble

The metamorphosis of an expanding bubble on top of a pillar into a mushroom-shaped bubble upon collapse is given in Figures 10–12 together with the pressure, velocity and flow fields in the liquid (water), respectively. The bubble starts with high internal pressure that drives the expansion of the bubble and gives rise to a radiated shock wave (frame 1 of Figure 10). At the circular edge of the pillar the shock wave is reflected with the emission of a low pressure acoustic torus wave. At about maximum expansion (frame 2 of Figure 10) the bubble is surrounded by a low pressure field.

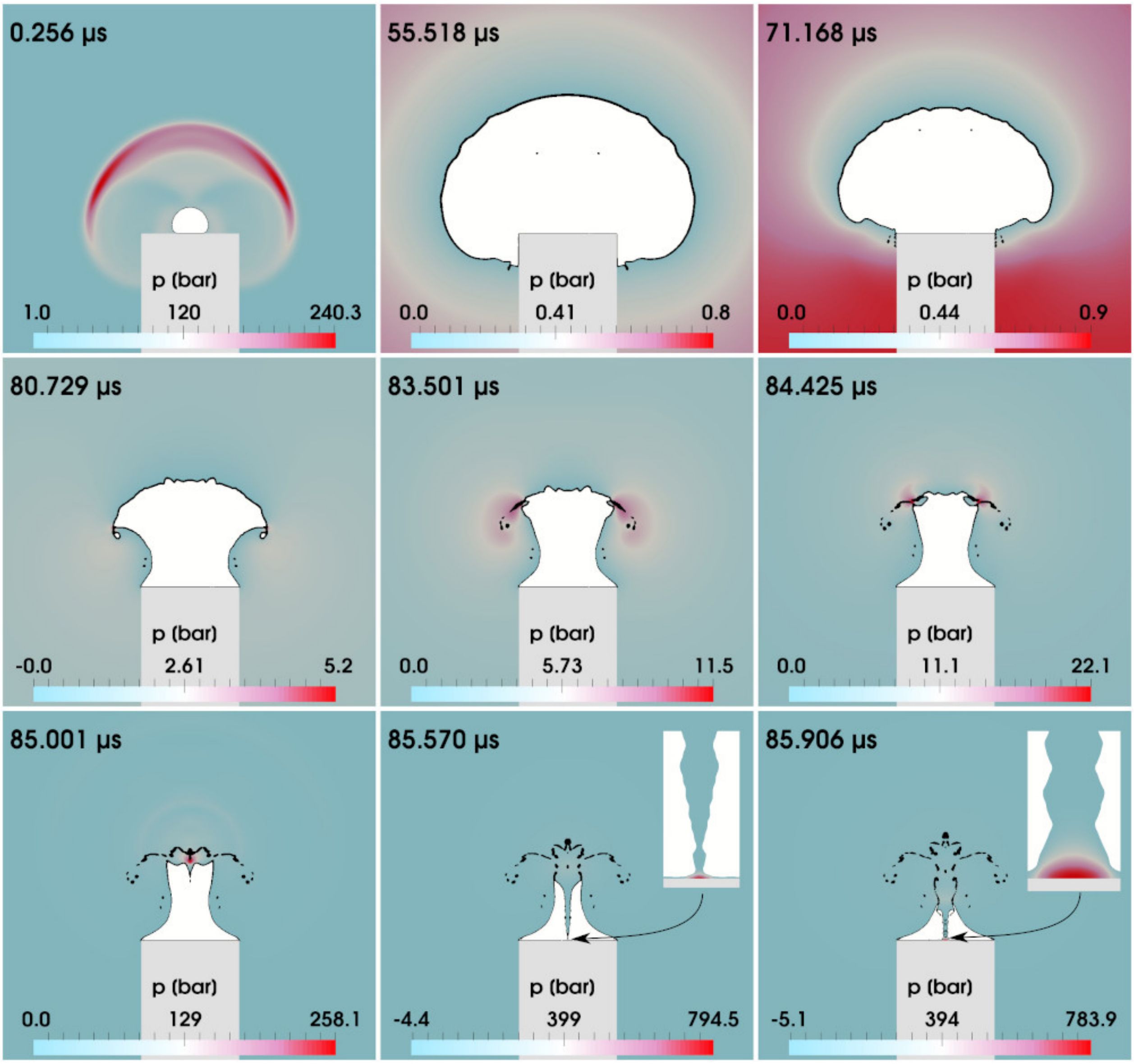

Figure 10. Simulation results for the pressure p [bar] of a bubble with $R_{\mathrm{max,unbound}} = 472.57\,\mu\mathrm{m}$, $D_{\mathrm{init}} = 30\,\mu\mathrm{m}$ and a cylinder radius of $r_{\mathrm{p}} = 200\,\mu\mathrm{m}$, resulting into $D^* = 0.06$ and $r_{\mathrm{p}}^* = 0.423$. White areas belong to the bubble. Cross sections along the center of axial symmetry. In the first frame (upper left frame), the shock wave from the bubble initiation is visible as is the low-pressure wave from diffraction at the rim of the cylinder. The last two frames contain a zoom inset into the region of maximum pressure at the flat top surface of the cylinder. Rayleigh collapse time T_{Rc} is 42.90 µs.

The collapse dynamics are best followed in the velocity-field sequence (Figure 11) and the warping of a color layer field that is advected with the flow (Figure 12). From the velocity distribution around the bubble in the second frame of Figure 11 it is seen that the collapse of the bubble starts from the overlap part of the bubble upwards. The flow is directed and guided upwards along the cylinder and at the rim of the cylinder inwards to form a gaseous stem and neck with a head. That way, the mushroom shape of the bubble is formed. At the sharp curvatures of the mushroom head high pressures are generated by liquid inflow through flow focusing (frames 5 and 6 in Figure 10). The ring-shaped pressure squeezes the top of the bubble head inwards towards the axis of symmetry. The self-impact of the flow leads to a fast jet downwards into the stem and a flow upwards, to be seen only later in time (Figure 12, last frame). Simultaneously, a small bubble may be left moving upwards. The collapse of the gaseous stem looks like receding downwards with leaving a foot stand (last frames in Figures 10–12). The foot stand collapses further and the upwards flow become visible together with a palmette-like flow structure with a stack of (torus) bubbles, as seen in Figure 12 (last frame).

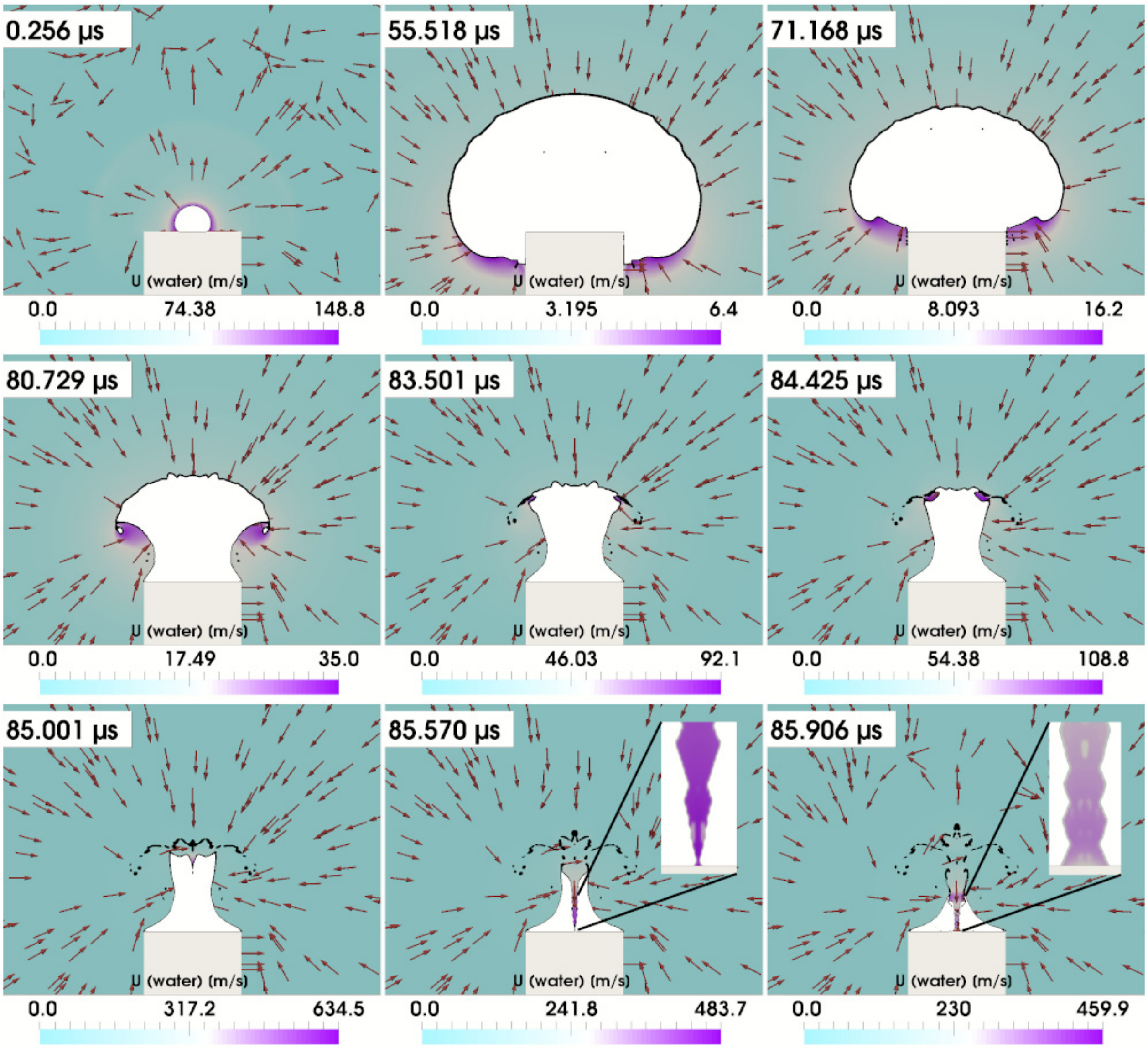

Figure 11. Simulation results for the velocity **U** of the same bubble and cylinder as in Figure 10. In the first frame (upper left frame), it is seen that the shock wave from bubble initiation induces an outward flow ahead of the expanding bubble surface. The last two frames contain a zoom inset into the region of maximum velocity (the fast jet). In the insets the velocity arrows are omitted for the sake of visibility. Cylinder radius is 200 μm.

Figure 12 shows a sequence of the warping of a color layer tracer field to make the liquid flow and layer mixing better visible in its entirety. It is observed that liquid is sucked upwards from below the cylinder sides already in the early collapse phase (frame 3 to 6 in Figure 12). The liquid for the fast jet derives from a liquid sheet just above the flat top of the cylinder (frame 7 and subsequent frames), whereas the liquid surrounding the receding neck derives from the liquid aside and below the cylinder (frame 4 and subsequent frames). The self-impact of the ring jet (between frame 6 and 7) not only leads to the fast jet downwards but also to a liquid jet upwards, as seen best in the last frame. Moreover, a peculiar palmette flow structure develops reminding of ornaments on antique ceramic vases.

The argument that there is indeed a fast jet in the experiments as well, is put in the following way: by comparing the simulations to the photographs of the experiment (e.g., in Figure 5, Figure 8 or Figure 9), it becomes evident, why there is no *neck closure* observed in the experiment. At first, the observer of the bubble in Figure 8 sees a tapering of the neck by about 1.2 pixels per 0.1 µs, so that a zero width is expected latest at 0.9 µs. Instead, a stable stem develops with a finite width. In the numerical simulations in 3D, shown later in Section 5.4, this stem can best be seen for comparison. When looking closely at a magnification of an intermediate frame of Figure 12 at $t = 85.906$ µs, shown in Figure 13, it is observable that the sideways inflow, denoted by the purple liquid layer, is hindered to reach the axis of symmetry by the fast-jet inflow denoted by the blue and almost black liquid layers.

The conclusion is therefore that the momentum of the fast jet seems to dominate the flow direction at the axis of symmetry due to the about twenty-fold velocity, even though the mass transported by the jet is supposedly much less than the one of the sideways inflow. Thus, the stable stem in the experiments can be explained by the phenomenon of the fast jet. In this respect, the fast jet is also seen in the experimental photographs, even though it is not evident to the eye without the knowledge of the simulations.

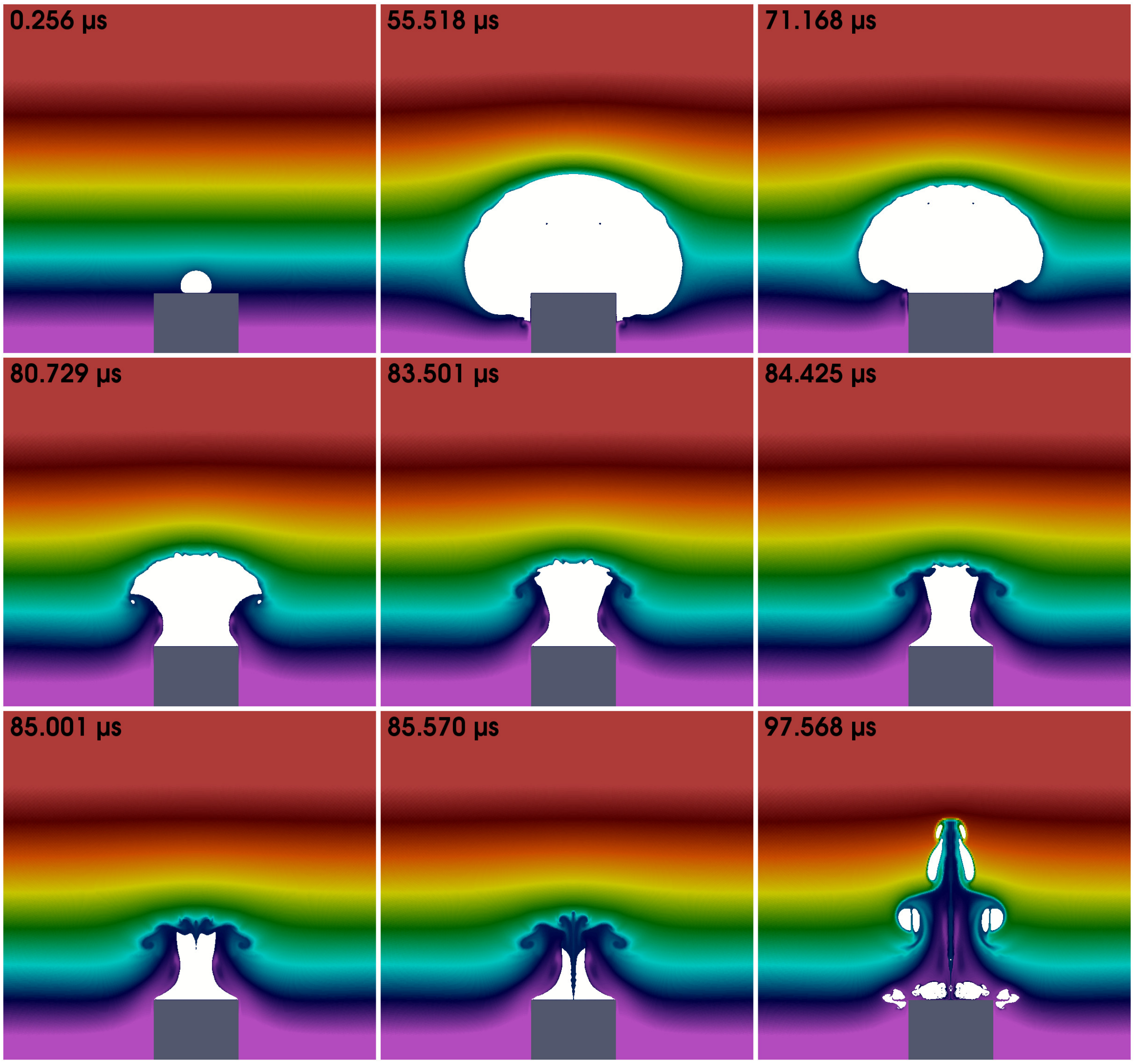

Figure 12. Flow field simulations presented with the help of a warped color layer tracer field of the same bubble and cylinder as in Figure 10. White areas belong to the bubble. Cross sections along the center of axial symmetry. Note the palmette-like flow structure in the last frame. Cylinder radius is 200 µm.

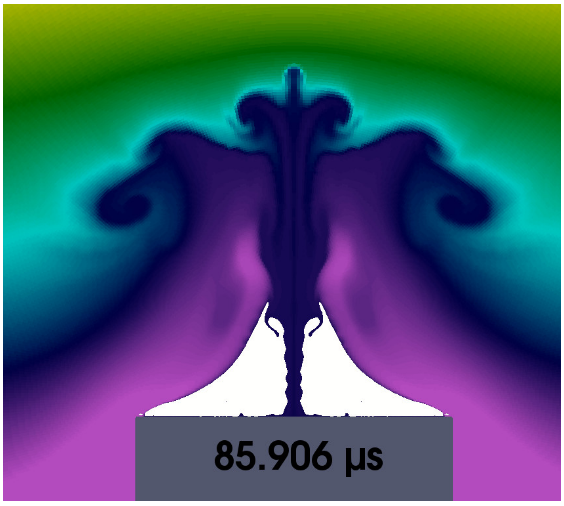

Figure 13. Enlargement of the bubble on top of the pillar at time 85.906 µs with the warped color layer tracer field of Figure 12. The white area is the bubble foot stand. It still collapses further. A stack of vortices develops from the upwards flow.

5.3. General Dynamics of a Mushroom Bubble

The general dynamics process of the formation of a mushroom-shaped bubble is explained in Figures 14 and 15 with a higher temporal resolution. It was found to be grossly similar for all D^*-cases investigated, as will be seen in Section 5.5.

In Figure 14, the typical expansion and begin of collapse of a bubble on top of a cylinder with $D^* \approx 0$ and $r_\mathrm{p}^* < 1$ (the radius of the cylinder is smaller than the maximum radius of a free bubble, $R_{\mathrm{max,unbound}}$) is shown. During expansion, when the bubble interface crosses the cylinder rim, it swirls around it, ejecting liquid droplets (in axial symmetry torus ring drops) into the bubble body. Once passed, these droplets hit the outer bubble wall, inducing surface waves there (dashed circles in frame 3). Due to the boundary layer around the cylinder, the bubble never touches the solid, but "swims" on the boundary layer. This is evident from simulations close to any solid boundary, but cannot be easily observed in the current experiment. However, there exists one measurement by Reuter et al. [96,97] for a bubble close to an extended plane solid boundary and a comparison with simulations by Lechner et al. [53] with excellent agreement.

When the bubble starts collapsing, the outer waist is lifted almost parallel to the cylinder. This flow produces the two annular inflows that form a) a neck and b) the extreme curvatures at the mushroom cap rim. As denoted by the red arrows and circles in frame 7, Figure 14, the flow that forms the mushroom neck has also a component upwards that tapers the cap to a thin gas film. The phenomenon of *flow focusing* comes into play [53,98], flow focusing generating strongest acceleration where curvatures are highest. An annular jet is formed that runs along the top part of the shrinking mushroom cap, leaving trails of dim remnant gas that form a thin umbrella. Numerically, this results into a tearing of the interface, leaving areas where $0.9 < \alpha_l < 1$. In the end, this annular liquid jet impacts in the zenith of the umbrella, producing a *fast jet*. The fast jet actually is the reason why the neck will not impact onto itself, as stated before concerning Figure 13. It can be seen in Figure 15 that the fast jet here reaches values of more than 700 m/s. In some cases, it is more than 2000 m/s, as will be shown later. The liquid inflow from the top now, starting from frame 1, Figure 15 on, makes all sideways inflows at the neck negligible, changing the subsequent dynamics to a zipper-like collapse. The neck is tapered from inside rather than from outside flows. In the experiment, only the aforementioned "bottom foot stamp" is observed here, because the outside bubble surface has too many wrinkles to see the jet inside. The minimum volume happens from top-down, thus the top gas fragments are already in the rebound phase, when the lower ones collapse and emit shock waves (not seen here – taking place in frame 7, Figure 15, as indicated by the dashed red circle in the frame). Therefore, the upper bubbles are "kicked" and squeezed upwards. Thereby, a layered structure of (torus) bubbles is observed.

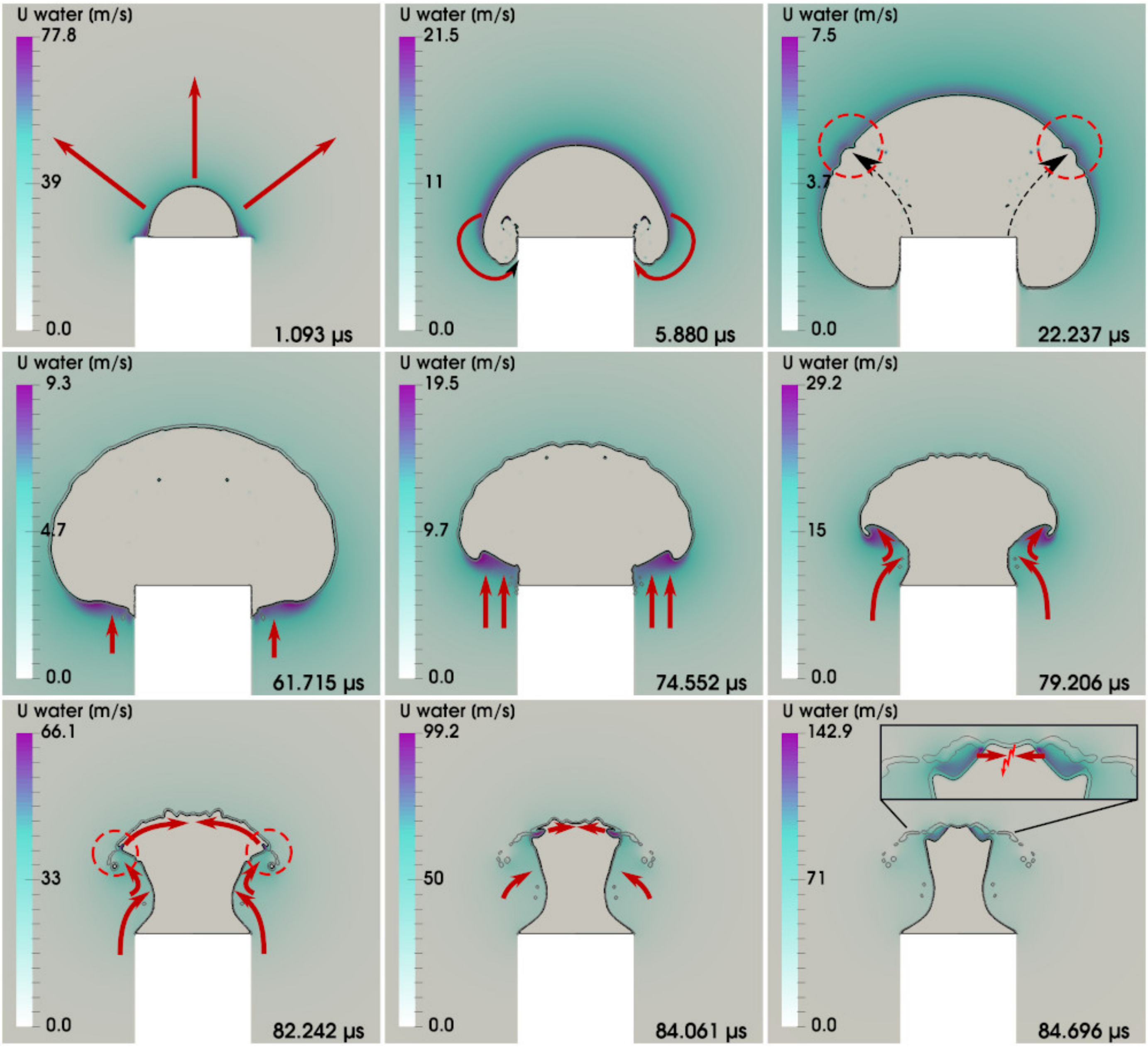

Figure 14. General dynamics of a mushroom bubble, part 1 shown using the same bubble as in Figures 10–13 ($R_{\mathrm{max,unbound}} = 472.57\,\mu\mathrm{m}$, $D^* = 0.063$, $r_{\mathrm{p}}^* = 0.423$, $T_{\mathrm{Rc}} = 42.90\,\mu\mathrm{s}$): expansion and begin of collapse, plotted with the modulus of the liquid velocity field. The red arrows indicate the essential directions of the flow field. The dashed red circles in the upper right frame indicate (torus) droplets that impinge onto the inner bubble wall. The dashed red circles in the lower left frame point to the area of the shedding of sub-resolution (torus) bubbles from the rim of the collapsing mushroom head. They finally form the umbrella left after collapse of the mushroom head. (see also Figure 15). Cylinder radius is 200 µm.

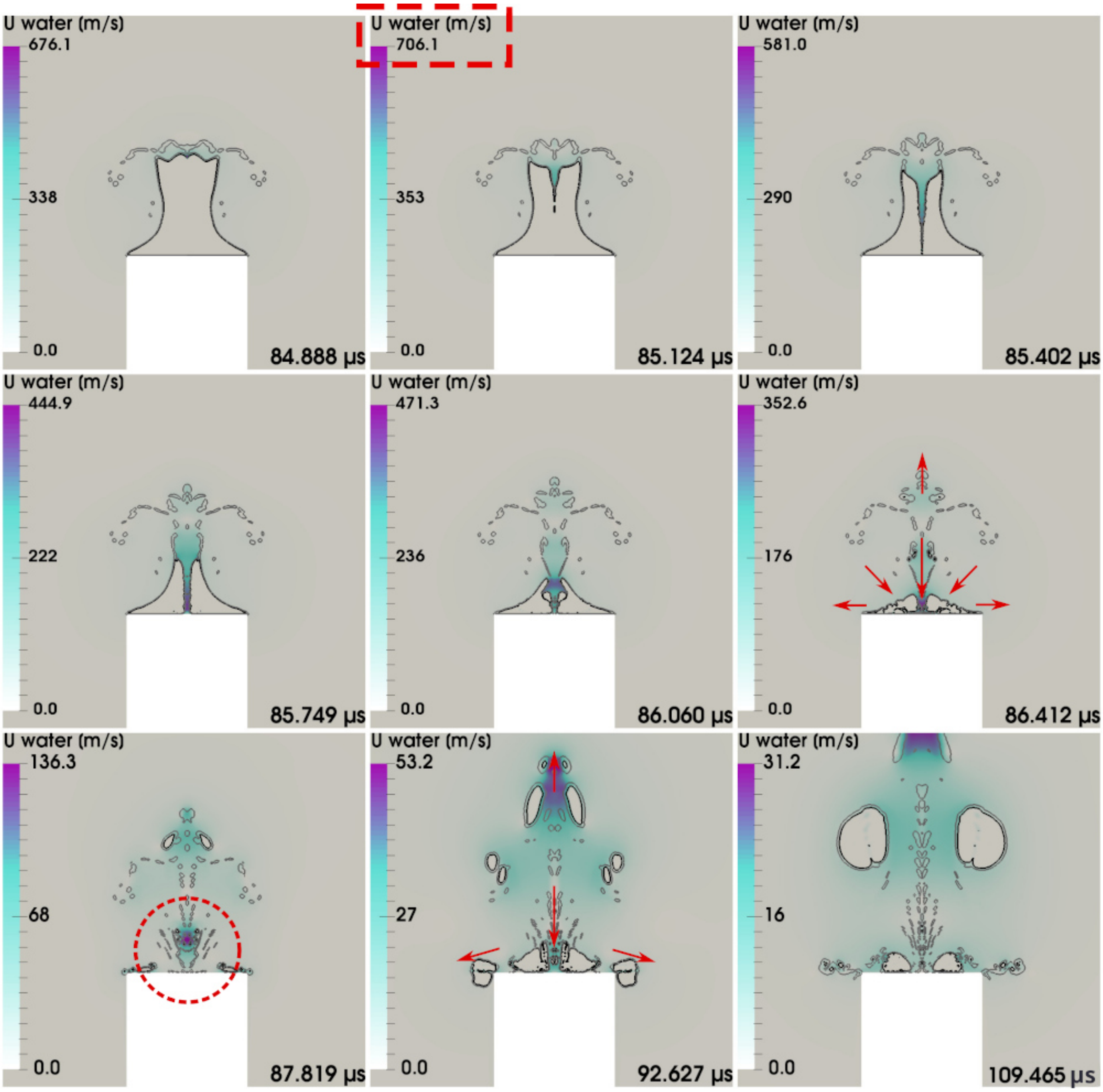

Figure 15. General dynamics of the mushroom bubble, part 2 ($R_{\text{max,unbound}}$ = 472.57 µm, D^* = 0.063, r_p^* = 0.423, T_{Rc} = 42.90 µs): fast jet formation, bubble collapse and rebound, plotted with the modulus of the liquid velocity field. The red arrows indicate the essential directions of the flow field. The fast jet in this case reaches more than 700 m/s (see dashed rectangle on top of the velocity scale in frame 2). The dashed red circles in the lower left frame denote the region, from where shock waves are emitted. Cylinder radius is 200 µm.

5.4. Simulation in Full 3D

One simulation is given in full 3D, i.e., without resorting to half or quarter spaces. Figure 16 shows an example—the dynamics of a mushroom bubble in a series of selected pictures plotted in a 3D view. It reveals that the axisymmetric calculations capture the main dynamics very well, in particular the mushroom shape and also the palmette-like bubble structure forming at and after collapse (the "projectile" experimentally, Figure 7).

A small calculation domain size has been chosen—a box of 10 mm edge length with the bubble in the center—to cope with calculation times. The contour surfaces of $\alpha_l = 0.9$ (light grey, transparent) and $\alpha_l = 0.5$ (green, transparent) are plotted. The higher value for α_l accounts for the dim gas remnants that are sub-resolution. They form the "umbrella" left after the collapse of the mushroom head (see Figures 14 and 15). The intention of the simulation was to show the qualitative agreement with the results in axial symmetry and the experimental observations.

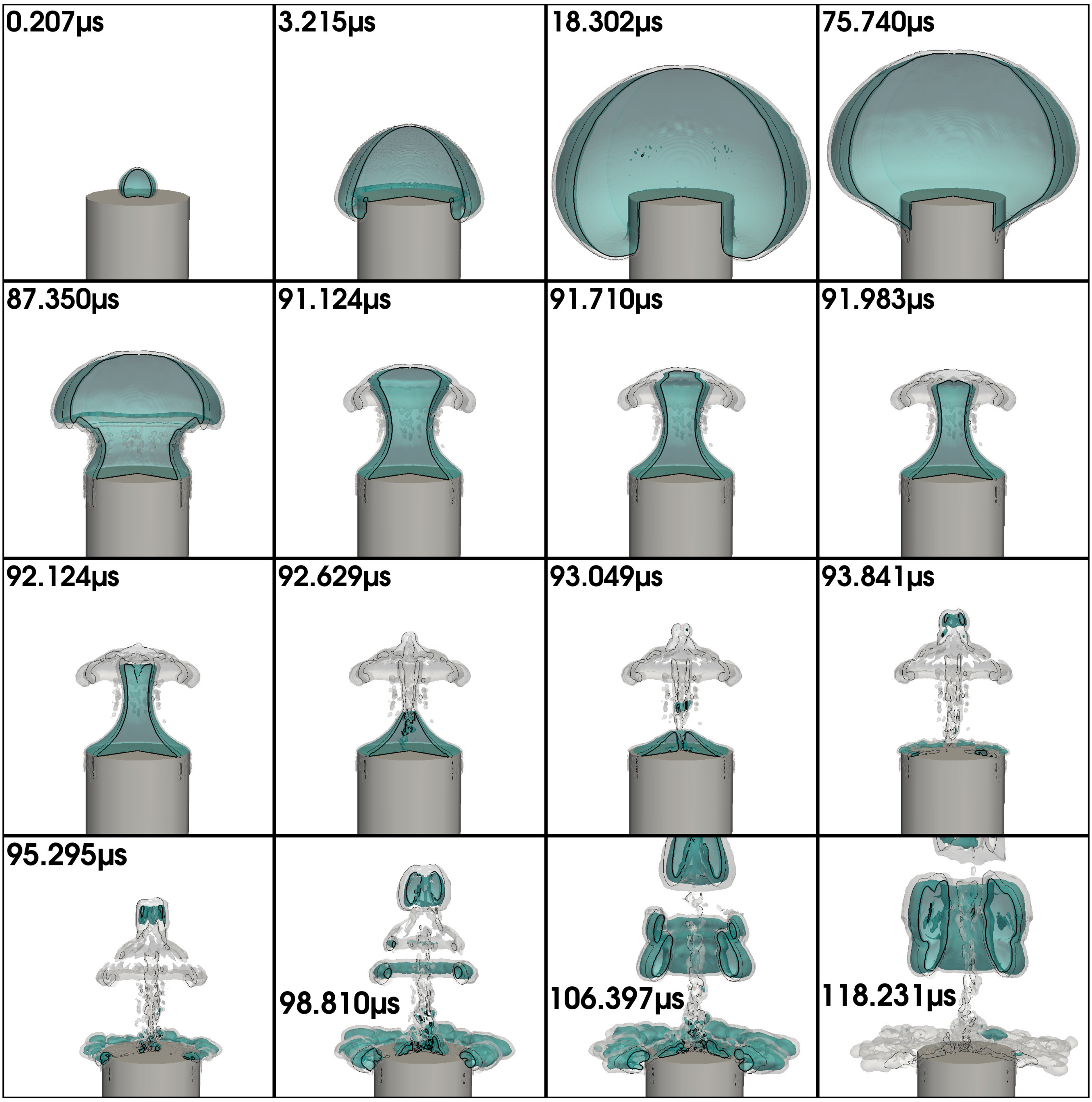

Figure 16. Full 3D simulation for $D^* = 0.057$, $r_\mathrm{p}^* = 0.382$ (large overlap of the bubble over the pillar rim), showing the "mushroom dynamics" including the projectile. Cylinder radius is 200 µm. The quarter volume of the bubble pointing to the front has been cut out for visualizing the bubble shape by a black contour line with the fast jet inside, first to be seen at 92.124 µs. The liquid is the white background for best visualization of the bubble and its contour.

It can be seen that the aforementioned torus-droplet splashing (Section 5.3) also takes place in 3D (frame 2 to 4, Figure 16), but the torus shape is broken to droplet fragments, as expected. This seems to be the main reason for asymmetric distortion of the bubble interface and the aforementioned wrinkles (Section 5.3).

5.5. Parameter Study

The parameter study is done with the intention to find the range in the two parameters D^* and r_p^*, where mushroom bubbles and their fast jets appear. A set of initial distances D_{init} = 30, 90, 150, 250, 350, 400 and 450 µm was chosen, as well as a set of bubble sizes determined, $R_{max,unbound}$ = 224.02, 249.98, 285.70, 333.32, 400.00, 472.57, 523.58 and 636.42 µm, generated by the respective initial radii of $R_{n,1}$ = 97, 105.20, 116.48, 131.52, 152.58, 175.5, 191.61 and 227.25 µm. From these sets, a subset of all combinations was chosen. The cylinder radius r_p was varied from 200 µm to 160 µm for the whole subset, as well. This results in a total of 89 cases studied. The specific values for $R_{n,1}$ and $R_{max,unbound}$ result from the conversion of the wanted values for r_p^* = 0.5, 0.6, 0.7 and 0.8 for $r_p = 200$ µm. The other values for $r_p^* < 0.5$ grew historically in the course of the study.

From this data set, Figures 17 and 18 show four examples of bubbles with mushroom dynamics for r_p^* = 0.423 and D^* = 0.063, 0.190, 0.317 and 0.529. The first row in Figure 17 shows the same bubble as in Figures 14 and 15, just for comparison. The bubbles are plotted with their liquid velocity field for four prominent time instances each in a row: 1—lifting the hips above the cylinder edge (after bubble maximum volume), 2—at about annular jet impact, 3—fast jet impact on the top of the cylinder and 4—at about bubble minimum volume. When looking at the equivalent radius at maximum volume of the mushroom bubbles, $R_{max,eq}$, it is seen that $R_{max,eq}$ tends to be smaller than $R_{max,unbound}$. As expected, some simulations showed that the bubbles lose their mushroom shape and approach a spherical shape at large D^* (refer to e.g., Figure A4). A complete description and scan of the transition region is left for future work.

The Figures 17 and 18 reveal, in their first column, that for bubbles close to the top of the cylinder the flow upon collapse is first directed upwards along the solid cylinder side to form a gaseous cylinder above it with a spherical cap larger than the gaseous cylinder diameter—the mushroom shape. With increasing length of the gaseous cylinder (the mushroom stem), the liquid flow along it is redirected inwards towards the axis of symmetry (as stated before concerning Figure 14). This redirection stems from the radial liquid inflow due to the bubble collapsing. In 68 of the 89 cases studied (five of them shown in Figures 17–19, as well as some more in Appendix E), the bubbles attain a mushroom shape on their way from their maximum volume to final collapse.

In the second column of the figures, the thick mushroom stem has developed into a neck, and the mushroom head has collapsed or almost collapsed by annular inflow of liquid. A characteristic feature of the collapse of the head is the formation of an "umbrella" of tiny bubbles. The umbrella persists some time with collapse of their bubbles and their rebound, as seen in the third and fourth column of the figure.

In the third column, a thin, fast jet has developed and reaches the cylinder surface. The maximum jet velocity surmounts 2100 m/s in some range of distances, for the current grid setup. For complete curves or manifolds of the jet velocity in dependence on the distance from the surface and on bubble and cylinder size, huge extra work would be necessary.

The jet velocity was found to depend on many factors for the mushroom case, e.g., the torus droplets that remain from the swirling of the bubble around the cylinder rim (see Figure 14, frame 2 and 3) and hinder the annular inflow. Furthermore, it was observed that remainders of these droplets can gather at the axis of symmetry and hinder the fast jet in its progression. The precise occurrence of these droplets is of rather chaotic nature and therefore extremely grid dependent. The velocities of the fast jets of the bubbles investigated range from 189 m/s to 2164 m/s and fluctuate by several 100 m/s per case, depending on the grid. It was already shown in [60] that the precise velocity of the fast jet for $r_\mathrm{p}^* \to \infty$ cannot be given yet, since it does not converge with increasing resolution in space and time.

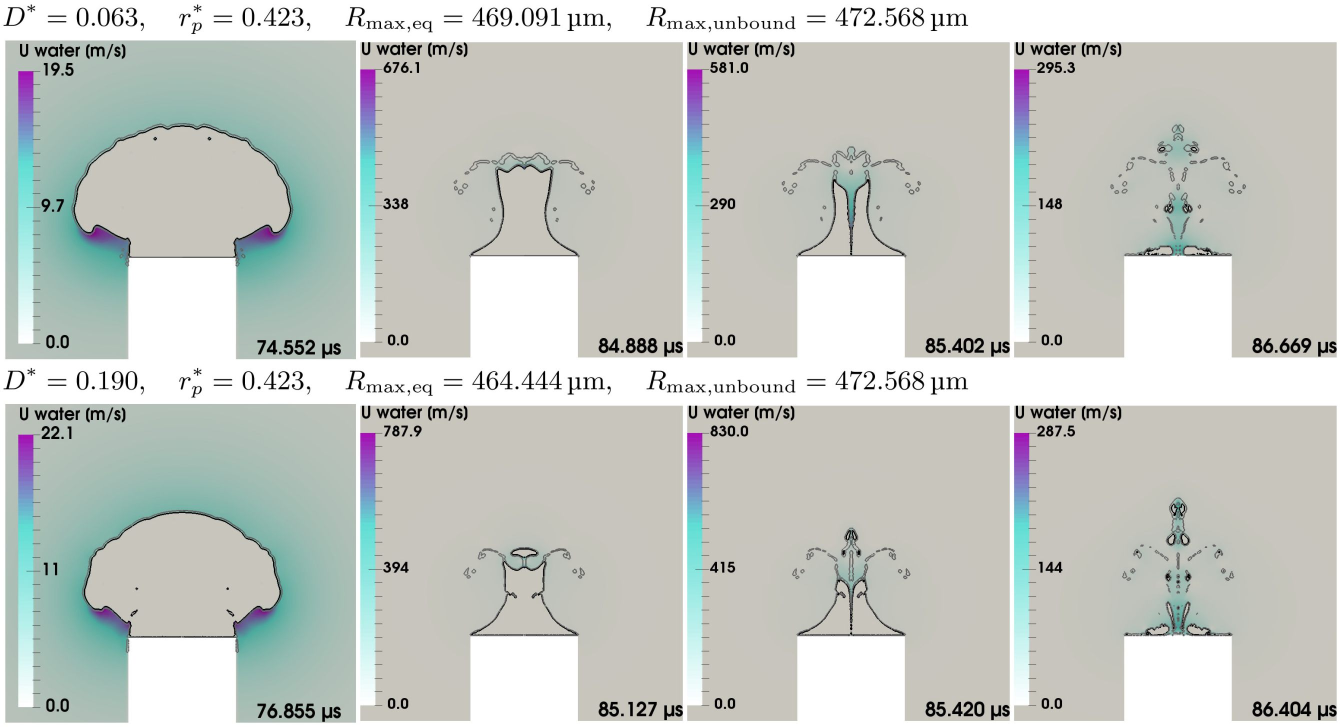

Figure 17. Mushroom bubbles with the magnitude of the flow velocity of the liquid. Bubbles at the same $r_\mathrm{p}^* = 0.423$ for two different normalized distances D^* with the same $R_{\mathrm{max,unbound}}$. The individual color scales give the maximum velocity in the respective frame. Note the small bubble in the second row, second frame, on top of the bubble stem and the stack of small (torus) bubbles that are shot upwards away from the pillar by the upwards flow after annular-flow impact (last column). They can be identified with the projectile in the experiment. When comparing with the experiment, note that the numeric pictures are presented as a cut through the bubble and should be complemented by rotation of the cut for a full bubble view. Cylinder radius is 200 µm.

In the fourth column of Figures 17 and 18, the mushroom stem has collapsed with small remains of the foot stand. The small bubbles of the umbrella are still present. The annular self-impact not only gives rise to the fast jet towards the pillar top, but also initiates a fluid flow in the opposite direction (see Figures 12 and 13). A stacked sequence of (torus) vortices is formed by the confined, jet-like upwards flow (Figure 13 and the lower row of Figure 15). Thereby, a vertically stacked sequence of bubbles develops.

The examples show mushroom bubble dynamics with (fast) jet formation by annular inflow with self-impact. Overall, it can be stated that the special type of mushroom-bubble formation, collapse and fast jet formation occurs in a large range of parameters, at least for bubbles on a long pillar. Over the parameter range studied, the only significant differences for the mushroom bubbles are the curvature of the outer interface of the mushroom stem at self-impact of the annular inflow, as well as the height of the stem at the time of fast jet formation.

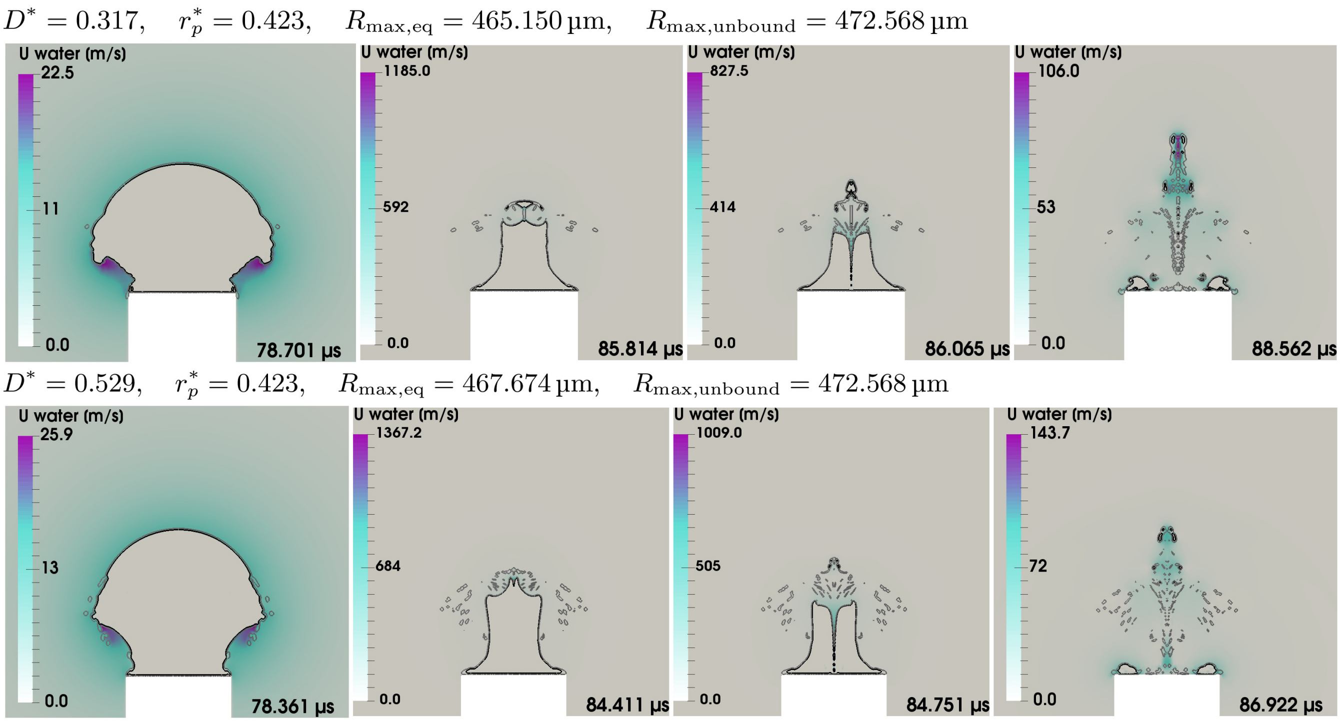

Figure 18. Mushroom bubbles with the magnitude of the flow velocity of the liquid. Bubbles at the same $r_{\mathrm{p}}^* = 0.423$ for two further normalized distances D^* with the same $R_{\mathrm{max,unbound}}$, in addition to Figure 17. Cylinder radius is 200 µm.

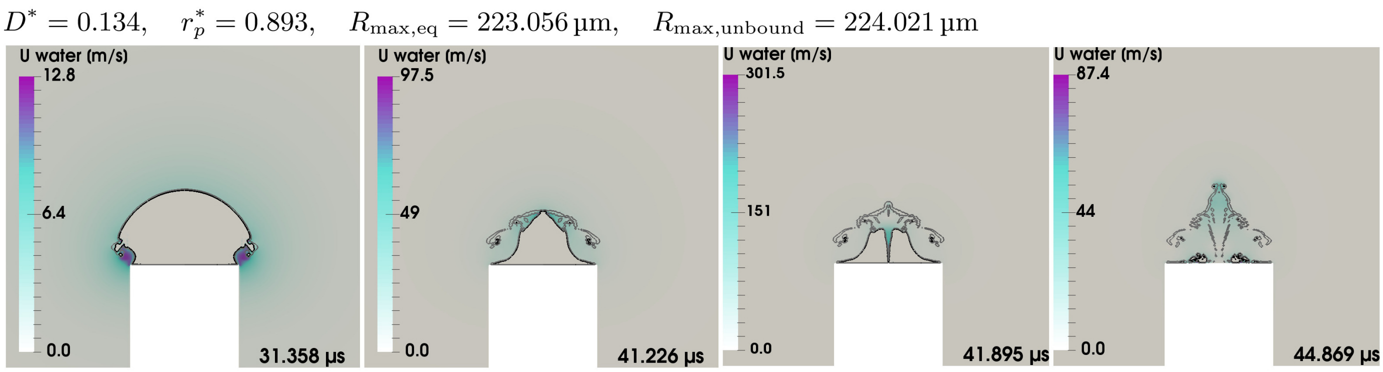

Figure 19. Mushroom bubble with the magnitude of the flow velocity of the liquid. Bubble at $r_{\mathrm{p}}^* = 0.893$ and $D^* = 0.134$. Very small overlap at maximum volume over the pillar rim. More examples with this r_{p}^* in Figure A4 in Appendix E. Cylinder radius is 200 µm.

In the present work it becomes evident that fast jet formation is not restricted to the case of bubbles very close to a surface of an extended solid as first found numerically in [53,60,61] and confirmed experimentally in [58,59]. What can be noted here, too, is that the parameter range, where a fast jet occurs, can be extended to at least $D^* = 0.875$ in the case of the mushroom bubbles, compared to $D^* = 0.2$ in the case of a bubble in the vicinity of a flat solid boundary ($r_{\mathrm{p}}^* \to \infty$).

Extending the parameter range to higher values of r_{p}^*, that is to bubbles with small or no overlap over the pillar rim at maximum volume, a minor change in bubble dynamics occurs. An example is given in Figure 19 for $r_{\mathrm{p}}^* = 0.893$ and $D^* = 0.134$ for a bubble with small overlap. The bubble hardly develops a mushroom shape (first frame). Only a broad short stem develops (second frame). But a fast jet with a velocity of 301.5 m/s develops with a receded stand foot (third frame). There are only few remains of a sort of mushroom head (fourth frame). Considering the results of Ref. [53] for a flat solid boundary (corresponding to $r_{\mathrm{p}}^* \to \infty$), it can be stated that for $D^* = 0.134$ and $r_{\mathrm{p}}^* > 0.893$ a fast jet will most probably occur, albeit not all of them being of the mushroom type. It is conjectured that there will be a gradual transition from a mushroom-type collapse to a "$r_\mathrm{p}^* \to \infty$"-type collapse [53] with both types exhibiting a fast jet. The results already show that annular-inflow-induced fast jets in bubble dynamics are a robust phenomenon.

Extending the parameter range to $r_\mathrm{p}^* \to 0$ is left to a future study. A complicated transition scenario is expected to other forms of bubble dynamics. The reason is that the bubble dynamics in free space is approached with an unknown transition scenario, as finally the mushroom bubbles must disappear. The study of this transition is beyond the scope of the present work.

Figure 20 shows results of the parameter study by means of an interpolated heat map with isocurves of the extracted quantities. The data points are plotted in their respective colors that represent their values. White data points denote cases, where either the bubble dynamics was different from the mushroom case or a standard jet by involution of the bubble wall was observed. The values of the velocities of the fast jet are given in Figure 20A, but they are to be understood as tentative results, since they are not converged values, as stated before. Variations in the jet velocity of up to several hundred meters per second were found, depending on the torus droplet-formation dynamics, grid structure and grid resolution. For evaluation of the velocity the definition given in [53] was applied: The velocity of the jet is defined by the distance from the location of the jet formation to the location of the jet impact onto the pillar surface divided by the time in between the two events. The corresponding water hammer pressures ($\rho\, c\, v_\mathrm{jet}$) would range from 0.3 GPa to 3 GPa. The time interval from fast-jet formation till the impact is given in Figure 20B. It is linked to the fast-jet velocity and therefore to be regarded as a tentative result. The only interpretation that can be drawn from Figure 20B is that the interval is in the range of 1 percent of the Rayleigh collapse time computed with Equation (3).

Four different quantities that seem more robust are given in Figure 20C–F. In Figure 20C the prolongation factor of the collapse time, the time from maximum bubble volume until the minimum volume, is shown, normalized by the Rayleigh collapse time. The prolongation factor seems to increase with increasing r_p^* and depend less on D^*.

In (Ref. [53], Figure 16) the prolongation factor for the case of a flat solid boundary is given as a function of D^* including experimental values. For the case of bubbles very close to the boundary ($D^* \to 0$), the prolongation factor reaches 1.27. In the case of mushroom bubbles, it is seen in Figure 20C that already for $r_\mathrm{p}^* \approx 0.9$ the value of 1.2 is obtained.

The maximum equivalent radius of the bubbles is smaller than $R_\mathrm{max,unbound}$ for all mushroom bubble cases but three, as shown in Figure 20D. For some cases at $r_\mathrm{p}^* > 0.8$ and $D^* > 1$ the relation $R_\mathrm{max,eq} > R_\mathrm{max,unbound}$ applies, too. However, the respective bubbles are not of a mushroom shape (refer to e.g., Figure A4).

In frame **E** and **F** the length of the jet is given, measured from the point of formation to the point of impact onto the pillar surface. When the jet length is put into relation to $R_\mathrm{max,unbound}$, it is seen that it approaches or exceeds the bubble maximum radius only for higher values of D^*. When the jet length is compared to the cylinder radius (Figure 20F), the jet becomes longer for smaller r_p^* as well (for a fixed r_p). The jet length varied by less than 10% with grid alterations. It could be an interesting quantity from an experimental point of view, when photographing the jet is planned.

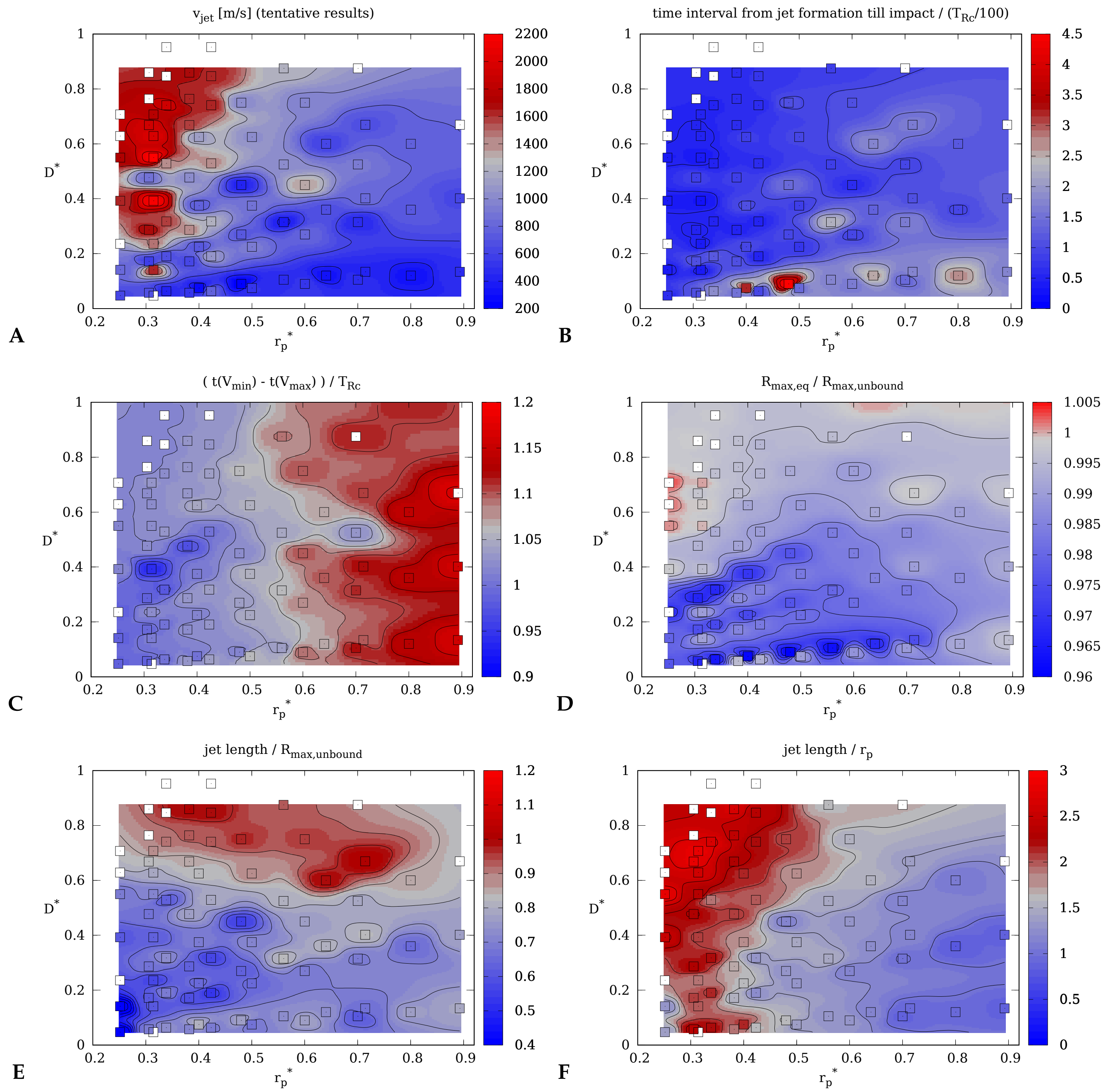

Figure 20. Extracted quantities from the parameter study including data points for both $r_\mathrm{p} = 160\,\mu\mathrm{m}$ and $r_\mathrm{p} = 200\,\mu\mathrm{m}$. Plotted are (**A**) the tentative results of the jet velocity for the given mesh (results may differ substantially for other meshes), (**B**) the tentative results of the time interval from jet formation till jet impact for the given mesh (results may differ substantially for other meshes), (**C**) the collapse time normalized by the Rayleigh collapse time, the number being called the prolongation factor, (**D**) the actual, equivalent maximum bubble radius normalized by $R_\mathrm{max,unbound}$, (**E**) the jet length normalized by $R_\mathrm{max,unbound}$, (**F**) the jet length normalized by the cylinder radius r_p. White data points denote cases, where either the bubble dynamics was different from the mushroom case or a standard jet by involution of the bubble wall was observed.

6. Discussion

The case of an expanding and collapsing bubble on top of a long cylindrical pillar on a plane solid boundary has been studied for the purpose of investigating whether the cylindrical constraint would provoke a fast jet as well. Experiments were done for bubbles very close to the flat top surface of the pillar ($D^* \approx 0$), with bubbles embracing the pillar top upon expansion. The accompanying numerical study is covering the cases of bubbles with diameters about two to three times the diameter of a very long cylinder and bubbles close to the flat top of the cylinder in the range $D^* = 0.047$ to $D^* = 2.009$. In 68 of the 89 cases studied, the bubble attains a mushroom shape with a fast jet into the stem and an oppositely directed flow that shoots a bubble cluster away from the pillar, the projectile (see Figure 7).

The previously published simulations where a fast jet occurs, were all done for bubbles close to or at an extended flat, solid boundary (i.e., $r_\mathrm{p}^* \rightarrow \infty$). The simulations in [53,58–60] were done with a small initial bubble of high internal pressure to simulate the expansion and collapse of laser-breakdown-induced bubbles (energy-deposit case [49]). The simulations in Pishchalnikov et al. [61], on the other hand, were done by inserting a bubble with prescribed shape and deliberate internal pressure into the liquid (a variant of the pure Rayleigh boundary case where a spherical bubble is inserted [49]). In the following, the results of Lechner et al. [53,60] and Pishchalnikov et al. [61] are compared: The prescribed-shape Rayleigh-boundary bubble in Ref. [61] was given the form of an oblate spheroid with a flat part at the solid boundary. This shape was derived from the photographed shape of a bubble oscillating in a sound field at the surface of a urinary stone. It is very reminiscent of the shape of an energy-deposit bubble at maximum volume after expansion very close to a solid surface [60] that expanded and collapsed at an ambient static pressure of p_∞ = 101,315 Pa. The Rayleigh-boundary bubble in Ref. [61] was made collapsing at p_∞ = 1.55 MPa, derived from the pressure of the acoustic field applied in the corresponding experiment. Given an internal pressure of P_{02} = 100 kPa (notation in [61]), a fast jet towards the solid boundary with a velocity of v_{jet} = 1164 m/s was found. When the (experimentally unknown) internal pressure is reduced to P_{01} = 10 Pa (almost empty bubble), a velocity of v_{jet} = 4117 m/s is obtained. In Ref. [53], fast-jet velocities of 1327.18 m/s for $D^* = 0.1$ and 2061.3 m/s for $D^* = 0.048$ were found. Because of too different conditions between Ref. [53,61], a quantitative comparison could not yet be done. It must be stated, too, that none of the above mentioned fast-jet velocities converged with higher grid resolution owing to the singular nature of the self-impact after annular flow focusing, even when viscosity (energy dissipation) and the compressibility of the liquid (energy storage) are included in the model.

Experimental results for the fast jet can be found in Benjamin Ellis [20], Pishchalnikov et al. [61], Koch [58] and Koch et al. [59]. In the following, the results therein are discussed. In Ref. [20], the bubble was subjected to highly reduced ambient pressure, which made it possible to photograph the slowed-down phenomenon already in 1966. In Ref. [61], an experimental bubble is shown developing the typical constriction upon collapse as also present numerically [60,61]. Direct comparisons of experimental and numerical bubble shapes show very good agreement up to the very collapse [61]. The fast jet was not caught in the experiment there, but when experiments and simulations fit over a large part of the dynamics, it is legitimate to interpolate the dynamics in between with the appropriate equations, here the Navier-Stokes equations (see the same arguments in [53] with examples). Thus it can be predicted from the numerical interpolation of the experimental collapse sequence that a fast jet was present in the experiment in Ref. [61].

Koch et al. [59] compared an experimental bubble with simulations over the whole cycle of expansion and collapse with a real camera and also a virtual camera by inserting the simulated bubble into a digitized version of the experimental setup. They could even catch the fast jet in the real experiment and with better resolution in the simulated experiment. With a spatial resolution of 1.8 µm, the full 3D simulation of the experimental bubble predicts a maximum jet speed of at least 732 m/s. The corresponding measurement of

Philipp and Lauterborn [12] amounted to 150 m/s as a lower bound owing to the limitations of the experimental instrumentation. When trying to compare the different jet speeds, the different experimental and numerical conditions must be respected. However, when extending the range of D^* towards higher values, the simulations of Supponen et al. [18], Lechner et al. [53] and Koch [58], as well as the experiments of Philipp and Lauterborn [12], Brujan et al. [96], Koch [58] and Koch et al. [59] can be compared as shown in Figure 21.

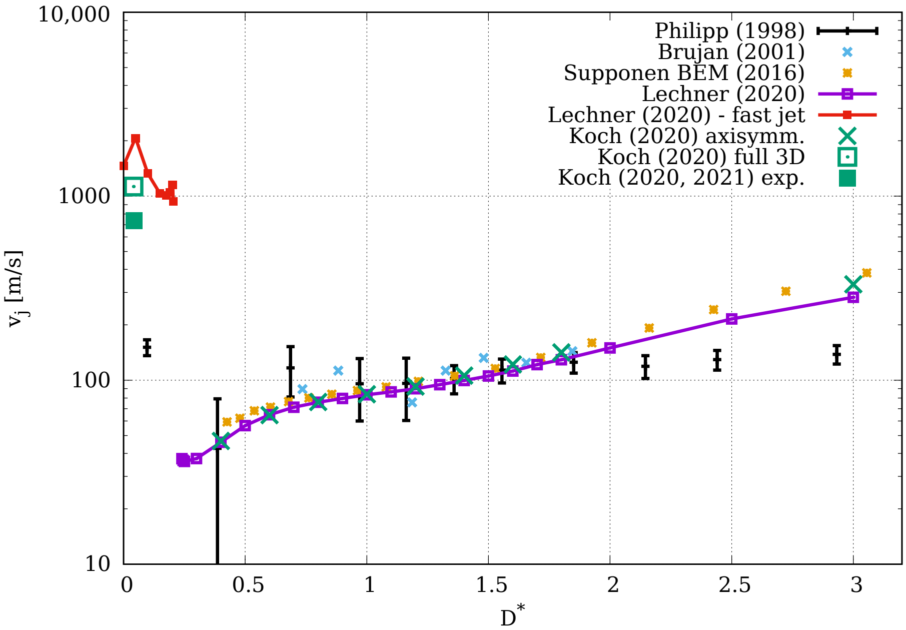

Figure 21. Jet velocities of a bubble in the vicinity of a flat solid boundary, measured and simulated by different authors: Philipp and Lauterborn [12] (measurements), Brujan et al. [96] (measurements), Supponen et al. [18] (Boundary Element simulation), Lechner et al. [53] and Koch [58] (simulations with the present code), as well as Koch [58] and Koch et al. [59] (measurement of the fast jet). The experimental data in [12,96] were obtained for laser-generated cavitation bubbles in water under normal ambient conditions ($p_\infty = 101325$ Pa and $\rho_l = 998\,\mathrm{kg/m^3}$). In the numerical work in [53,58,59], the same ambient conditions were assumed. The dimensionless values given in [18] have been incorporated into this diagram, using the values $\Delta p = p_\infty - p_v$ with p_∞ = 101,325 Pa, $p_v = 2337$ Pa and $\rho_l = 998\,\mathrm{kg/m^3}$.

The diagram of Figure 21 shows the jet speeds of (expanding and) collapsing bubbles obtained on flat solid boundaries given in dependence on the normalized distance, D^*, of the bubble to the boundary. There is excellent agreement over large part of the diagram (D^* up to 2) with deviations only where the limits of instrumentation were approached (about 150 m/s). There is an interesting experimental point at D^* = 0.1 with v_{jet} = 150 m/s. According to the numerical simulation, it well could have been a fast jet, just off the experimental possibilities at that time. The measurements repeatably gave this unexpected off-lying high value at the limit of instrumentation.

When comparing the fast jets on pillars here with the fast jets on a plane solid boundary in [53], it is noticed that the range of fast jet formation with respect to the normalized distance D^* is extended to at least $D^* = 0.875$. For a plane solid boundary, the range is restricted to below $D^* \approx 0.2$ [53]. The reason for the extension of the range of fast jets in the case of pillars seems to be the liquid that additionally is sucked up by the collapsing bubble from aside and below the top of the pillar. After having passed the flat top the liquid is redirected towards the axis to eventually form the neck. The liquid flow, via neck formation, produces a sharp curvature by constriction of the at first spherical cap to form the mushroom head. By flow focusing in the course of the proceeding collapse, an accelerating annular inflow is generated. During the proceeding annular inflow, the numerical approach of an interface with finite thickness comes in favour, since it indicates the flat sheets of gas in the mushroom umbrella that are sub-resolution. Upon self-impact of the annular inflow, the bubble is divided into a very small bubble on top and the main bubble below that sits on the top of the pillar. Simultaneously, a thin, fast jet is generated into the gaseous stem (see Figures 10–13), while bubble collapse still progresses. Interestingly, the liquid of the fast jet stems from the liquid above the top line of the pillar, whereas the liquid around the gaseous stem originates from liquid aside and below the top of the pillar (Figures 12 and 13).

The upwardly directed momentum of the liquid from neck formation pushes the remains of the bubble head upwards as best seen in Figure 4 for an experimental bubble and in Figure 16 for a numerical 3D-bubble. The final formation mechanism for the fast jet is the same as with a plane solid boundary, but owing to a different history in forming the sharp curvature at the rim of the mushroom head. The sharp rim is only formed in the course of *collapse* of the bubble, whereas in the case of a plane solid boundary it is formed upon *expansion* of the bubble by the viscous boundary layer [53].

Due to the singular event of the impact of the annular inflow, the numerical results of the present work are not evaluated for the exact numbers of the fast-jet velocities. The focus of this work is on mushroom-bubble dynamics and the comparison towards experimental photographs, as well as proving the existence of the fast jet in the case of bubbles above pillars. Thereby a second type of fast jet formation by annular inflow with self-impact has been found. It is coupled to the development of the mushroom shape, in particular to the sharp curvature of the rim of the mushroom head.

Mushroom-like dynamics like the ones presented here can be found, for instance, in Tomita et al. ([10], Figure 14b), Palanker et al. [82], Li et al. [78,80] and Zhang et al. [79]. In all those works, single cavitation bubbles are investigated close to curved, rotationally symmetric objects. However, those authors were only interested in the whole bubble cycle rather than the collapse details as in the present work. In Ref. [10], the authors investigate different solid-boundary curvatures and in the case of high curvatures the bubble shape is close to the shapes in the case of a cylinder. The bubble was generated at $D^* \approx \gamma = 0.33$ on top of a convex object with a curvature radius slightly larger than the bubble maximum radius. In comparison to the present work, it seems that the bottom foot stand (see Figure 7) of the mushroom shape is missing and the stem has a rather cone shape. This shape is reminiscent of the bubble in Figure 19 that for larger r_p^* is on the way to shapes at a flat solid boundary. This comparison persists for the other works, too. The authors of Ref. [82] investigated a similar structure as the previous authors for the purpose of investigating the application for eye surgery. The bubble in their work is generated on top of a pencil-like electrode and the subsequent dynamics looks very similar to the ones that is presented here. However, the authors focus on the phenomenon occurring much later than the first bubble collapse, called "jet" in their work and "projectile" in the present work. The authors of the Refs. [78–80] investigate bubbles close to rigid spheres of similar size as the bubble. It seems that the bubble shape that is given in the present work, which includes the bottom foot stand and the straight stem, is determined by the sharp edge of the cylinder object. According to our experience (Figure 19) with bubbles of similar sizes of bubble and object, they do not develop a real mushroom shape with a long stem. However, interpreting the dynamics visible in the above works, it could be guessed that a fast jet might occur there as well, because of the formation of a mushroom-like cap and the inevitable, following flow focusing.

A nearby sharp edge can lead to interesting phenomena in the early stages of bubble evolution, as has been investigated experimentally by Senegačnik et al. [86]. A secondary cavity can form directly below the edge caused by the low pressure region of the bubble induced overflow of the liquid over the edge. Albeit our model does not include phase transition, we notice the formation of a low pressure region directly below the edge (not shown). Furthermore, using diffuse illumination, Senegačnik et al. [86] visualize and measure the liquid injection into the bubble that follows the expansion of the bubble over the sharp edge (see Figure 14).

Another example of an annular liquid inflow is given by a bubble trapped in a narrow gap [77]. The jet velocities, however, stay below 200 m/s, probably due to the flow restriction of the liquid domain.

For micro-sized bubbles (radius 1 µm) Zevnik et al. [81] find very different shapes in dependence on the distance from a solid sphere and on the sphere size. It can be deduced from the radius-over-time curves of the bubbles that the collapse is not very strong. This may be the cause for the different dynamics without a fast jet. The higher influence of surface tension for smaller bubbles leads to high internal pressures in the bubble at rest and thus a cushioning of the collapse.

As a result of the study, it can be stated that different preconditions may initiate bubble shapes that provoke a converging annular inflow with self-impact and fast jet formation.

7. Conclusions

A laser-induced bubble on top of a long cylinder with a radius at maximum volume larger than the radius of the cylinder shows a dynamics very different from a bubble on an extended flat surface. After having embraced the cylinder top upon expansion, upon collapse it develops a mushroom shape with a head, a long stem and a footing. The special fluid flow leading to the mushroom shape could be reproduced in numerical studies by solving the Navier-Stokes equations for a Tait-compressible liquid with OpenFOAM. The simulations were carried out in axial symmetry (2D), as shown sufficient by comparison with a simulation in full 3D. The simulation code has been validated again by comparison of an experimental with a numerical mushroom shape (Figure 9). Moreover, the code has been compared with other, independent codes with respect to jet velocities (Figure 21). The bubble model has been validated by comparison with a complete high-speed experimental sequence comprising bubble expansion, the first collapse, the rebound and the second collapse of a laser-induced bubble with $D^* = 1.6$ in the vicinity of a flat solid boundary (Figure A1). A quite large range of parameters has been studied ($0.047 \leq D^* \leq 2.009$ and $0.251 \leq r_\mathrm{p}^* \leq 0.893$). In 68 of 89 cases investigated, the bubble forms a mushroom shape and the mushroom head collapses with forming a fast jet (velocity ranging from 189 m/s to 2164 m/s) into the gaseous stem from the self-impact of an annular inflow by two-dimensional flow focusing. The existence of the fast jet in the experiments has been proven by comparing the experiments with the numerical simulations with respect to stem stability. The mixing of the liquid by the bubble has been shown by warping of a color layer tracer field that is advected with the flow. The range of parameters shows that fast jets of annular-inflow type (studied numerically in [53,60,61] and experimentally in [58,59] for bubbles close to a plane solid boundary) are not a singular phenomenon, but rather a robust one. It is expected to occur in many other configurations as well, and to alter the view on cleaning and erosion of surfaces. It may find applications in laser-induced ablation in liquids with pillars of various shapes as targets for laser synthesis and processing of colloids [99]. The fast jet phenomenon also bears a clear potential for erosion of solids, since the water hammer estimates reach to several GPa.

Author Contributions: M.K. and W.L. led and conducted the overall research. J.M.R. contributed to the experimental part, C.L. contributed to the numerical part. R.M. contributed to the conceptualization and provided funding. All authors contributed to the writing and reviewed the paper. All authors have read and agreed to the published version of the manuscript.

Funding: The work was funded in part by the Deutsche Forschungsgemeinschaft (DFG, German Research Foundation) under projects Me 1645/8-1 and Me 1645/8-3, the Austrian Science Fund (FWF) (Grant No. I 5349-N) and the Alexander von Humboldt Foundation (Germany) through a Georg Forster Research Fellowship.

Institutional Review Board Statement: Not applicable.

Informed Consent Statement: Not applicable.

Data Availability Statement: No data available.

Acknowledgments: The authors thank the Cavitation Bubble Dynamics Group at the Drittes Physikalisches Institut, Universität Göttingen, for many inspiring discussions, especially B. Lindinger for the inspiration to use light passing through the bubble as a camera trigger. The authors also thank the workers of the workshops and the IT support at the Drittes Physikalisches Institut for their constant support and they furthermore thank Francisco Jimenez for the fruitful exchange of experience with certain solver control parameters. The authors acknowledge support by the Open Access Publication Funds of the Göttingen University.

Conflicts of Interest: The authors declare no conflict of interest.

Appendix A. Mass Reduction of the Bubble, Validation of the Bubble Model

The phenomenon of laser-induced breakdown to produce a bubble is not modelled in the present work. Instead, an initial bubble of high internal pressure is taken that expands to the experimental maximum radius. The condensation of the vapour part in the bubble is modelled by a reduction of the radius at rest of the bubble, R_n. Hentschel and Lauterborn [95] stated that good agreement between the Gilmore model and experiments is found, when the equilibrium radius R_n of the bubble is reduced by 60% at the time when the bubble is at maximum radius. In the present work, this approach was incorporated by a linear reduction of R_n from $R_{n,1}$ to $R_{n,2}$ in the time interval between t_a and t_b:

$$R_n = R_n(t) = \begin{cases} R_{n,1} & t < t_a \\ (t - t_a) \cdot (R_{n,2} - R_{n,1})/(t_b - t_a) + R_{n,1} & t_a \le t < t_b \,. \\ R_{n,2} & t > t_b \end{cases} \tag{A1}$$

The density of the bubble is changed in the same manner as it is changed during the global mass correction step (see Appendix B), after the new m_0 has been determined:

$$m_{0,\mathrm{new}} = m_0 \cdot \left(\frac{R_n(t)}{R_{\mathrm{n},1}} \right)^3$$

$$\rho_{g,\mathrm{new}}(\mathbf{x}, t) = \frac{m_{0,\mathrm{new}}}{m(t)} \rho_g(\mathbf{x}, t)$$

The values of $R_{n,1}$ and $R_{n,2}$ in this work are chosen as follows: for fixed R_{init}, $R_{n,1}$ is a parameter that is varied for different initial bubble energies and hence different maximum radii the bubble expands to. Akhatov et al. [91] gave experimental data on the rebound radius compared to the maximum radius of a bubble in unbounded liquid. When fitting these data with the present code, the following relation is found:

$$R_{n,2} = 0.127 R_{\mathrm{max,unbound}} \approx 40\% \, \frac{1}{3.1662} R_{\mathrm{max,unbound}}, \tag{A2}$$

confirming the assumption of Hentschel and Lauterborn [95] and the factor in Equation (9). In the present work, however, $R_{n,2}$ was chosen to be fixed at 64 µm due to historical reasons.

This method to reduce the gas content during simulation has been validated by comparison with experiments. As an example, Figure A1 shows a comparison between experiment and numerical simulation for a bubble next to a flat solid boundary with $D^* = 1.6$. Shown are the first collapse, the first rebound and the second collapse. Very good agreement is found concerning the shape and size of the bubble as functions of time. Simulation parameters are $R_{n,1} = 184\,\mu\mathrm{m}$, $R_{n,2} = 64\,\mu\mathrm{m}$ for a bubble with $R_{\mathrm{max,unbound}} = 500\,\mu\mathrm{m}$, where the gas content has been reduced according to the above method with $t_a = 30\,\mu\mathrm{s}$ and $t_b = 40\,\mu\mathrm{s}$. Without reduction of R_n, the numerical bubble would lose less energy at the first collapse, resulting in a much larger maximum volume at rebound than in the experiment.

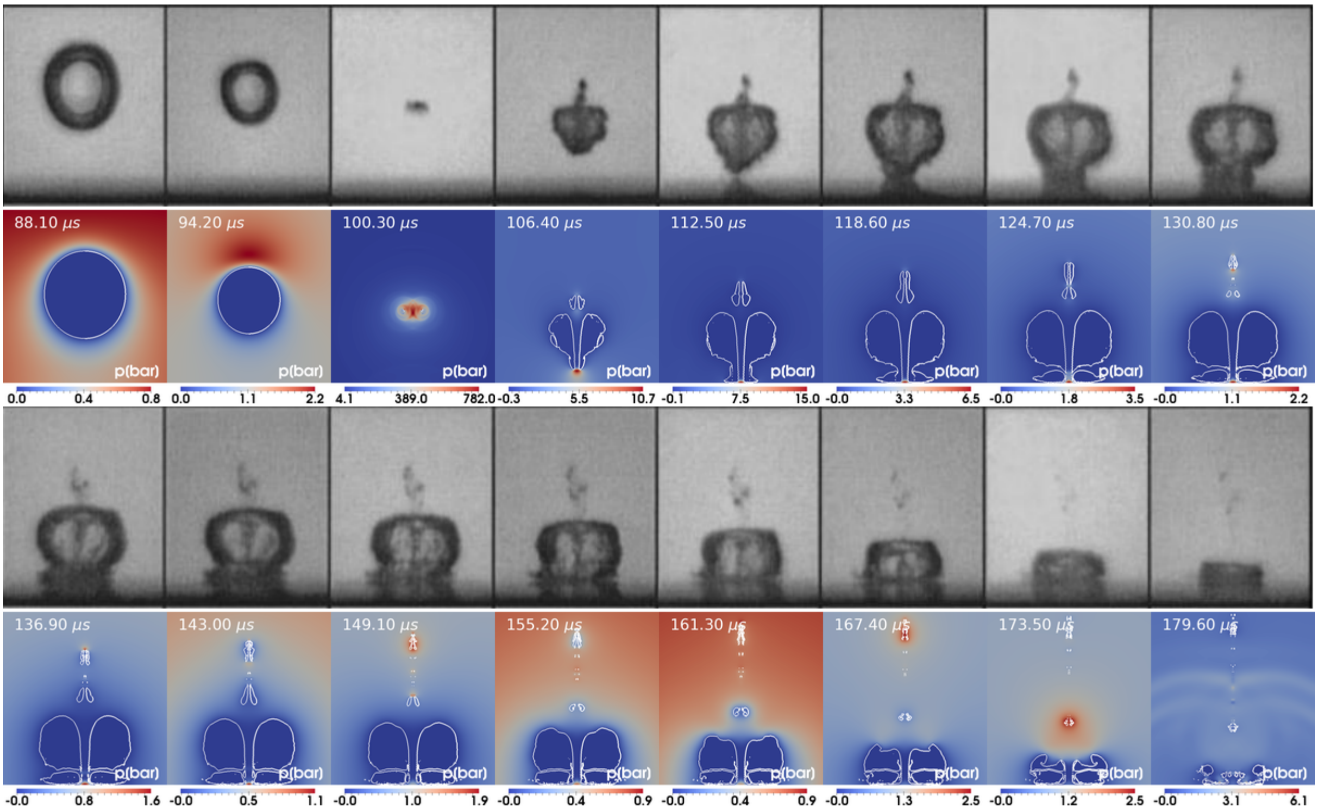

Figure A1. First collapse, rebound and second collapse of a bubble next to a flat solid boundary with $D^* = 1.6$. Comparison of experiments ([12], Figure 2d) and numerical simulations. Experiment: High-speed pictures in gray scale. Time between frames $\Delta t_{\text{exp}} = 17.7$ µs, $R_{\text{max,exp}} = 1450$ µm, frame width = 3.9 mm. Numerical simulation: The color represents the pressure in bar. The white line indicates the interface (liquid volume fraction $\alpha_l = 0.5$). Time between frames 6.1 µs, $R_{\text{max,sim}} = 500$ µm, frame size 1.345 mm × 1.42 mm (width × height). The solid boundary is located at the lower border of each frame. Simulation with surface tension set to zero, $\sigma = 0$.

Appendix B. Mass Error Compensation

It was noted already in [42,94] that due to the segregated nature of the solver, the mass of the bubble undergoes an error over time. We apply two versions of compensation. Both of them are applied after the last iteration of the pressure equation.

Global mass correction

This approach has been described in [42]. The density in each cell of the gas phase simply is multiplied by the ratio of the initial bubble mass to the current bubble mass:

$$\rho_{g,\text{new}}(\mathbf{x}, t) = \frac{m_0}{m(t)} \rho_g(\mathbf{x}, t).$$

This approach has been validated by comparison to the Gilmore model and to experimental data also in axial symmetry in [42]. It has been proven to work very well until the first collapse and slightly longer. The disadvantage is that, when the bubble gets fragmented, each of the fragments is treated the same, regardless of the pressure inside the fragment.

Local mass correction

This approach aims to compensate the error where it occurs. After the last iteration of the pressure equation, the continuity equation for the gas is reconsidered in the form

$$\frac{\partial \tilde{\alpha}_g \rho_g}{\partial t} + \nabla \cdot \left(\tilde{\alpha}_g \rho_g \mathbf{U}\right) = 0$$

and solved for the field $\tilde{\alpha}_g \rho_g$. The gas density ρ_g is obtained from the field $\tilde{\alpha}_g \rho_g$ by division by $\tilde{\alpha}_g$, where $\tilde{\alpha}_g$ is a copy of the field α_g with

$$\tilde{\alpha}_g = \begin{cases} 0.999 & \alpha_g \geq 0.999 \\ 0.001 & \alpha_g \leq 0.001 \\ \alpha_g & \text{else} \end{cases}$$

in order to avoid division by zero. This approach has been validated by direct comparison of simulations in axial symmetry and full 3D to experiments in [58,59].

Appendix C. Initial Conditions

Initially, a spherical bubble with high internal pressure is placed at a distance D_{init} from the top of the cylinder in a still liquid under ambient pressure p_∞. The liquid volume fraction is set to

$$\alpha_l(\mathbf{x}_P, 0) = \begin{cases} 1 & \text{for} \quad (\mathbf{x}_P - \mathbf{x}_0)^2 > R_{\text{init}}^2 \\ 0 & \text{for} \quad (\mathbf{x}_P - \mathbf{x}_0)^2 \leq R_{\text{init}}^2, \end{cases}$$

with $\mathbf{x}_P$ denoting the center of a grid cell and $\mathbf{x}_0$ the initial center of the bubble. The initial volume of the bubble due to discretization is then determined as

$$\widetilde{V}_{\text{init}} = c \sum_{\mathbf{x}_P} (1 - \alpha_l(\mathbf{x}_P, 0)) V_P, \tag{A3}$$

where V_P denotes the volume of the grid cell P and c corrects for the wedge geometry of the mesh in case of an axis-symmetric simulation ($c = 1$ in a 3D simulation and $c = 360/\delta$ for a 2D simulation on a wedge with opening angle δ). The initial pressure in the bubble now is calculated by

$$p_g = p_n \left(\frac{R_n^3}{\tilde{R}_{\text{init}}^3} \right)^\gamma, \tag{A4}$$

where $\tilde{R}_{\text{init}}$ denotes the radius of the equivalent, perfect sphere with volume $\widetilde{V}_{\text{init}}$, i.e., $\tilde{R}_{\text{init}} = (3\widetilde{V}_{\text{init}}/(4\pi))^{1/3}$. The pressure and velocity field then are initialized as

$$p(\mathbf{x}_P, 0) = p_g\big(1 - \alpha_l(\mathbf{x}_p, 0)\big) + p_\infty \, \alpha_l(\mathbf{x}_P, 0), \qquad \mathbf{U}(\mathbf{x}_P, 0) = 0.$$

By applying the intermediate step Equation (A3) before step Equation (A4), the consistency between pressure and volume is maintained, that was slightly broken due to discretization. A perfect sphere of radius 20 µm and $R_n = 175.5$ µm, for example, would have a gas pressure of 927 MPa. When discretizing this sphere with cells of 1 µm edge length, the radius changes to 20.063 µm, resulting into a gas pressure of 915 MPa, i.e. 1.3% difference.

Appendix D. Calculation of the Advected Color Layer Map

A scalar field Γ was advected passively with the velocity field by a transient advection equation for incompressible flows:

$$\frac{\partial \Gamma}{\partial t} + \nabla \cdot (\Gamma \mathbf{U}) - (\nabla \cdot \mathbf{U})\Gamma = 0. \tag{A5}$$

It was initiated varying only in y-direction and thus as color layers when applying an adequate color map of Γ. The validity of the method was investigated in [58]. The initial data of Γ are set to:

$$\Gamma = \begin{cases} \dfrac{y}{1.5 \cdot R_{\max}} & y < 1.5 \cdot R_{\max} \\ 1 & \text{else} \end{cases},$$

for the center of the bubble in $\mathbf{x} = (0, 0)$.

Appendix E. Further Parameter-Study Plots

Here, further results on mushroom bubbles and other bubble types are given that contributed to Figure 20.

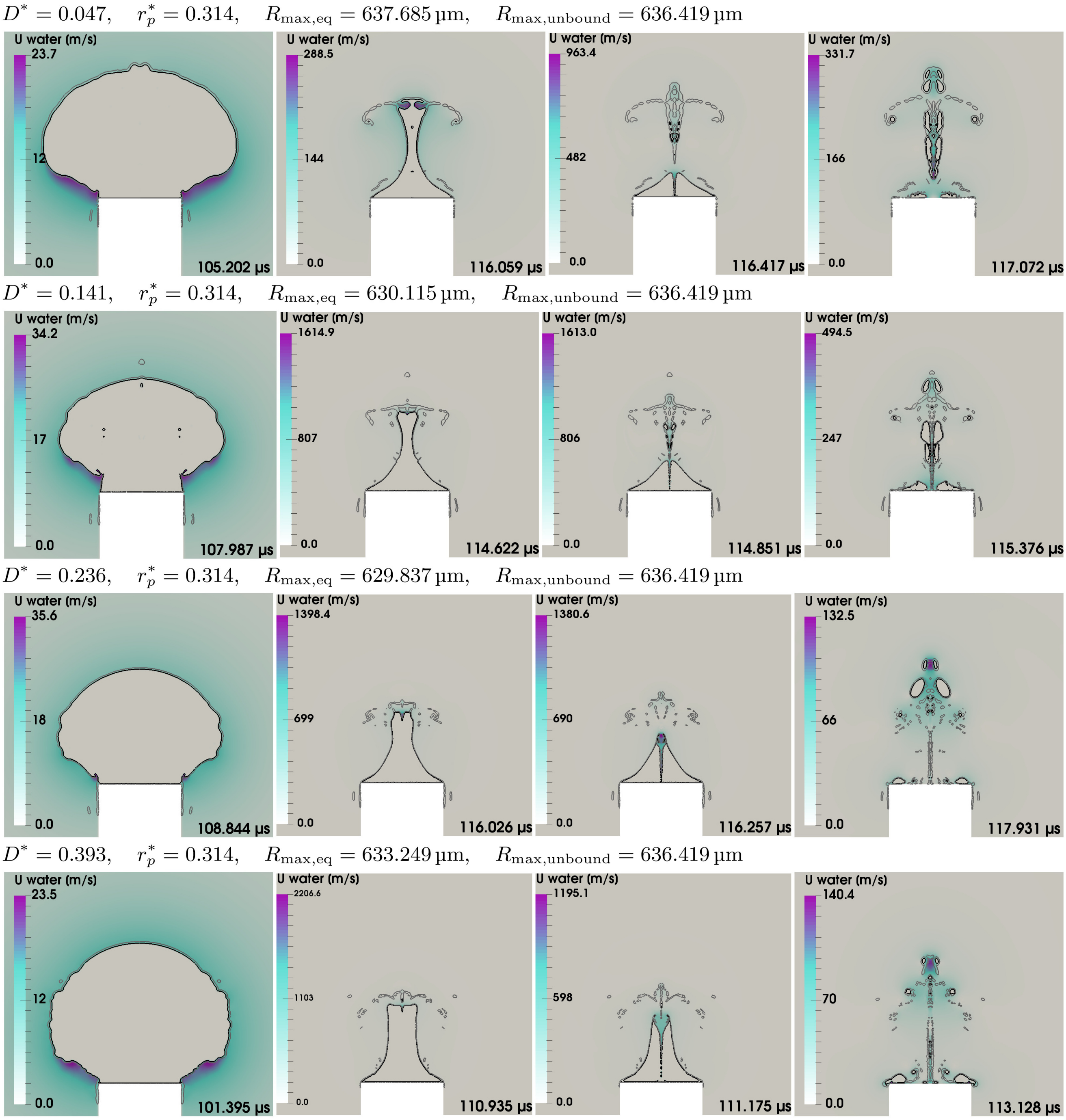

Figure A2. Mushroom bubble at $r_p^* = 0.314$ for four different normalized distances D^* with the same $R_{\max,\mathrm{unbound}}$. Cylinder radius is 200 µm. Large overlap at maximum bubble volume over the pillar rim. At large overlap and small D^*, the mushroom stem gets long and slim (see the experiments). Note the stack of (torus) bubbles that is shot upwards away from the pillar (last column).

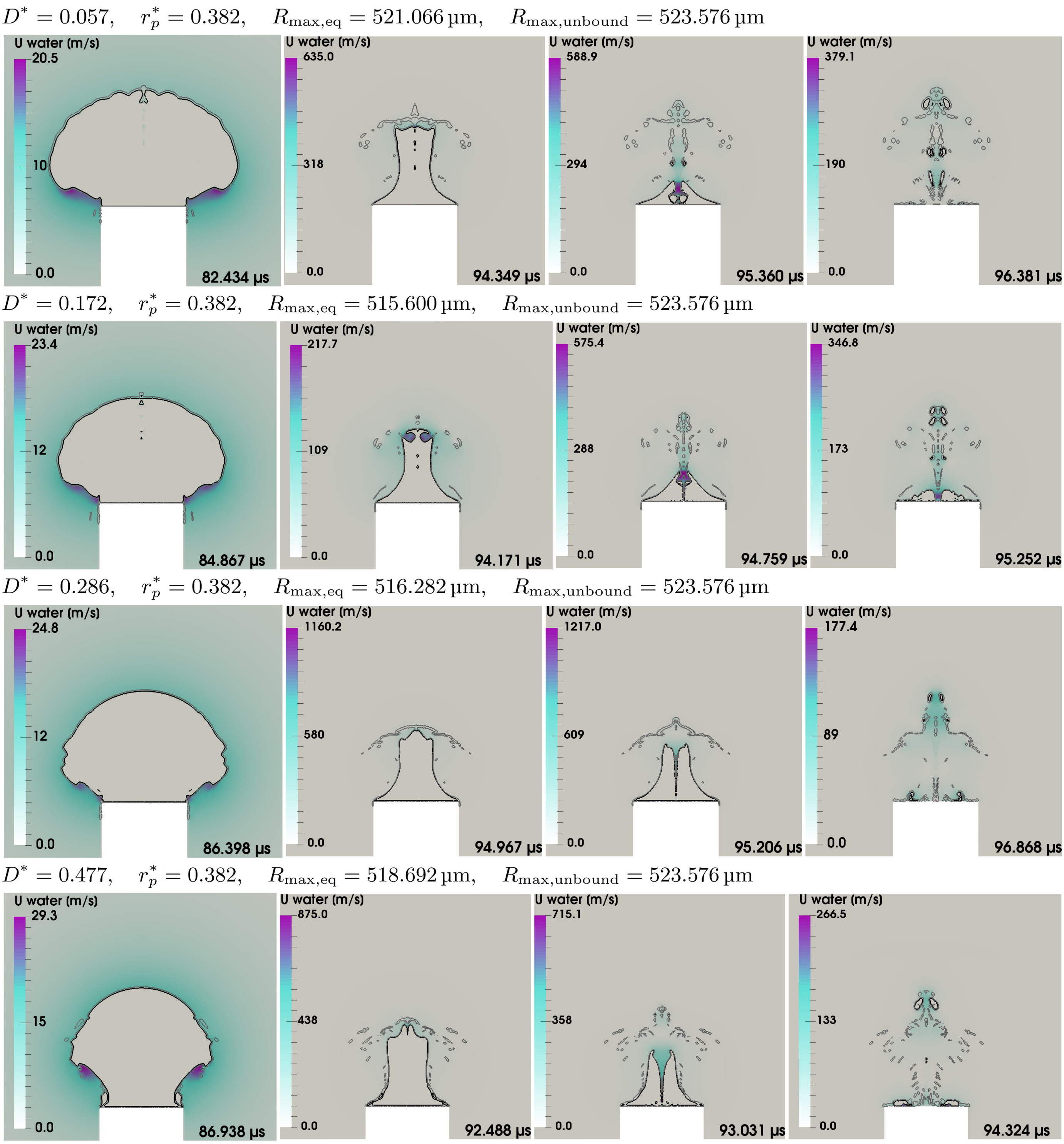

Figure A3. Mushroom bubble at $r_\mathrm{p}^* = 0.382$ for four different normalized distances D^* with the same $R_{\mathrm{max,unbound}}$. Cylinder radius is 200 µm. Less overlap than in Figure A2.

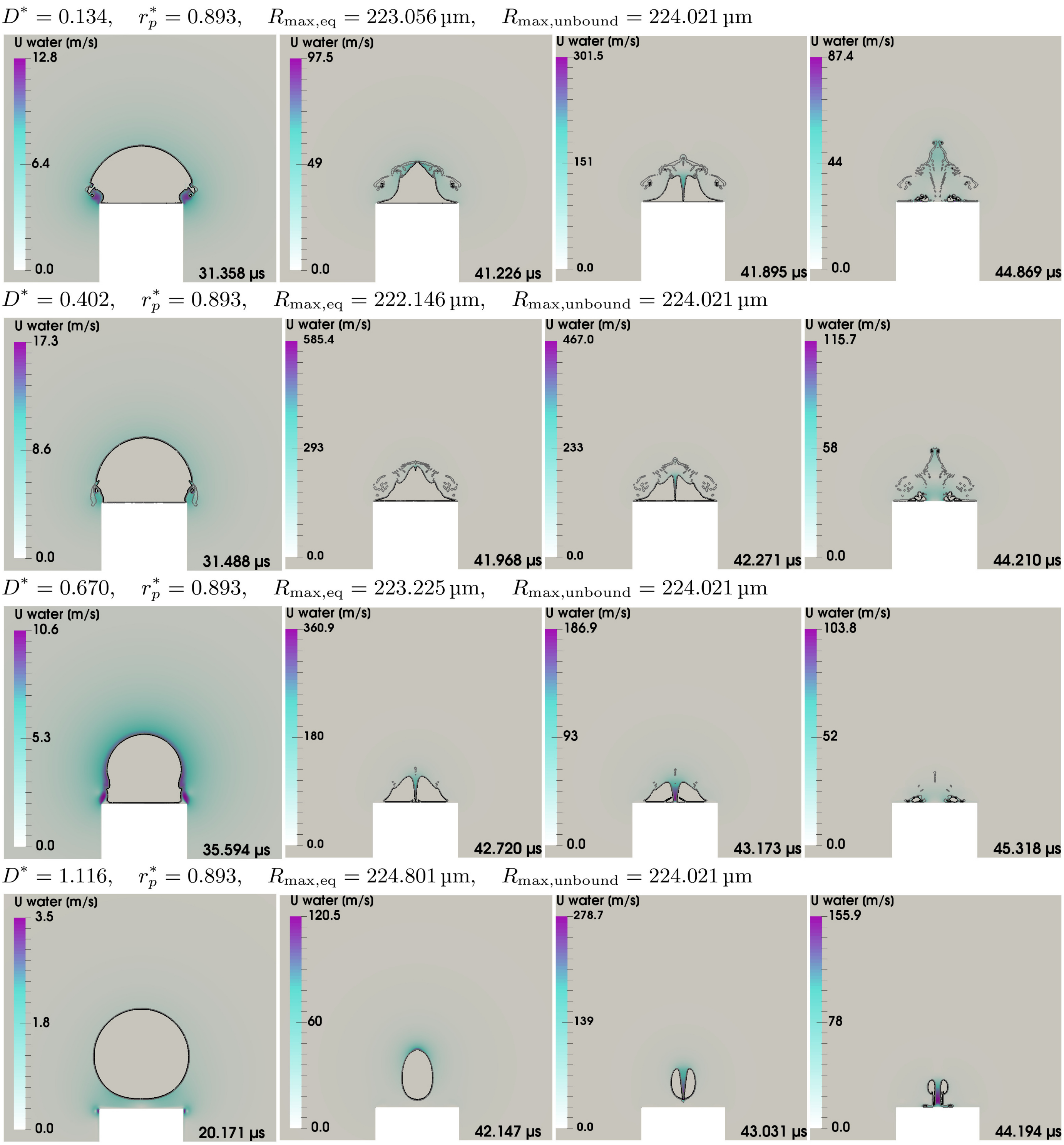

Figure A4. Mushroom bubble at $r_p^* = 0.893$ for two different normalized distances D^* with the same $R_{\text{max,unbound}}$. Very small overlap at maximum volume of the bubble over the pillar rim, no overlap for D^*= 1.116. The mushroom shape is gradually abandoned with increasing distance of the bubble from the pillar top. At least the jet in the last row is a standard jet with involution of the distal part of the bubble and not by annual inflow with self-impact. Cylinder radius is 200 µm.

References

1. Brennen, C.E. *Cavitation and Bubble Dynamics*; Oxford University Press: New York, NY, USA, 1995.
2. Kornfeld, M.; Suvorov, L. On the destructive action of cavitation. *J. Appl. Phys.* **1944**, *15*, 495–506. [CrossRef]
3. Leighton, T.G. *The Acoustic Bubble*; Academic Press: London, UK, 1994.
4. Lauterborn, W.; Kurz, T. Physics of bubble oscillations. *Rep. Prog. Phys.* **2010**, *73*, 106501. [CrossRef]
5. Askar'yan, G.; Prokhorov, A.; Chanturiya, I.; Shipulo, G. The effects of a laser beam in a liquid. *Sov. Phys.—JETP* **1963**, *17*, 1463–1465.
6. Felix, M.; Ellis, A. Laser-induced liquid breakdown—A step-by-step account. *Appl. Phys. Lett.* **1971**, *19*, 484–486. [CrossRef]
7. Lauterborn, W.; Bolle, H. Experimental investigations of cavitation-bubble collapse in the neighbourhood of a solid boundary. *J. Fluid Mech.* **1975**, *72*, 391–399. [CrossRef]
8. Lauterborn, W. Optic Cavitation. *J. Phys. Colloques* **1979**, *41*, C8-273–C8-278. [CrossRef]
9. Tomita, Y.; Shima, A. High-Speed photographic observations of laser-induced cavitation bubbles in water. *Acustica* **1990**, *71*, 161–171.
10. Tomita, Y.; Robinson, P.B.; Tong, R.P. Growth and collpase of cavitation bubbles near a curved rigid boundary. *J. Fluid Mech.* **2002**, *466*, 259–283. [CrossRef]
11. Blake, J.R.; Taib, B.B.; Doherty, G. Transient cavities near boundaries. Part 1. Rigid boundary. *J. Fluid Mech.* **1986**, *170*, 479–497. [CrossRef]
12. Philipp, A.; Lauterborn, W. Cavitation erosion by single laser-produced bubbles. *J. Fluid Mech.* **1998**, *361*, 75–116. [CrossRef]
13. Tong, R.P.; P., S.W.; Shaw, S.J.; Blake, J.R.; Emmony, D.C. The role of 'splashing' in the collaspe of a laser-generated cavity near a rigid boundary. *J. Fluid Mech.* **1999**, *380*, 339–361. [CrossRef]
14. Brujan, E.A.; Keen, G.S.; Vogel, A.; Blake, J.R. The final stage of the collapse of a cavitation bubble close to a rigid boundary. *Phys. Fluids* **2002**, *14*, 85–92. [CrossRef]
15. Lindau, O.; Lauterborn, W. Cinematographic observation of the collapse and rebound of a laser-produced cavitation bubble near a wall. *J. Fluid Mech.* **2003**, *479*, 327–348. [CrossRef]
16. Wang, Q. Multi-oscillations of a bubble in a compressible liquid near a rigid boundary. *J. Fluid Mech.* **2014**, *745*, 509–536. [CrossRef]
17. Koukouvinis, P.; Gavaises, M.; Supponen, O.; Farhat, M. Simulation of bubble expansion and collapse in the vicinity of a free surface. *Phys. Fluids* **2016**, *28*, 052103. [CrossRef]
18. Supponen, O.; Obreschkow, D.; Tinguely, M.; Kobel, P.; Dorsaz, N.; Farhat, M. Scaling laws for jets of single cavitation bubbles. *J. Fluid Mech.* **2016**, *802*, 263–293. [CrossRef]
19. Brujan, E.A.; Nahen, K.; Schmidt, P.; Vogel, A. Dynamics of laser-induced cavitation bubbles near an elastic boundary. *J. Fluid Mech.* **2001**, *433*, 251–281. [CrossRef]
20. Benjamin, T.B.; Ellis, A.T. The Collapse of Cavitation Bubbles and the Pressures thereby Produced against Solid Boundaries. *Philos. Trans. R. Soc. Lond. Ser. A* **1966**, *260*, 221–240.
21. Koukouvinis, P.; Gavaises, M.; Supponen, O.; Farhat, M. Numerical simulation of a collapsing bubble subject to gravity. *Phys. Fluids* **2016**, *28*, 032110. [CrossRef]
22. Obreschkow, D.; Tinguely, M.; Dorsaz, N.; Kobel, P.; de Bosset, A.; Farhat, M. The quest for the most spherical bubble: experimental setup and data overview. *Exp. Fluids* **2013**, *54*, 1503. [CrossRef]
23. Naudé, C.F.; Ellis, A.T. On the mechanism of cavitation damage by nonhemispherical cavities collapsing in contact with a solid boundary. *J. Basic. Eng.* **1961**, *83*, 648–656. [CrossRef]
24. Crum, L.A. Surface oscillations and jet development in pulsating bubbles. *J. Phys. Colloques* **1979**, *41*, C8-285–C8-288. [CrossRef]
25. Plesset, M.S.; Chapman, R.B. Collapse of an initially spherical vapour cavity in the neighbourhood of a solid boundary. *J. Fluid Mech.* **1971**, *47*, 283–290. [CrossRef]
26. Blake, J.; Taib, B.; Doherty, G. Transient cavities near boundaries: II. Free surface. *J. Fluid Mech.* **1987**, *181*, 197–212. [CrossRef]
27. Blake, J.R.; Hooton, M.C.; Robinson, P.B.; Tong, R.P. Collapsing cavities, toroidal bubbles and jet impact. *Proc. R. Soc. Lond. Ser. A* **1997**, *355*, 537–550. [CrossRef]
28. Blake, J.R.; Tomita, Y.; Tong, R.P. The art, craft and science of modelling jet impact in a collapsing cavitation bubble. *Appl. Sci. Res.* **1998**, *58*, 77–90. [CrossRef]
29. Blake, J.R.; Keen, G.S.; Tong, R.P.; Wilson, M. Acoustic cavitation: the fluid dynamics of non-spherical bubbles. *Philos. Trans. R. Soc. Lond. Ser. A* **1999**, *357*, 251–267. [CrossRef]
30. Vogel, A.; Lauterborn, W.; Timm, R. Optical and acoustic investigations of the dynamics of laser-produced cavitation bubbles near a solid boundary. *J. Fluid Mech.* **1989**, *206*, 299–338. [CrossRef]
31. Tomita, Y.; Shima, A. Mechanisms of impulsive pressure generation and damage pit formation by bubble collapse. *J. Fluid Mech.* **1986**, *169*, 535–564. [CrossRef]
32. Zhang, S.; Duncan, J.H.; Chahine, G.L. The final stage of the collapse of a cavitation bubble near a rigid wall. *J. Fluid Mech.* **1993**, *257*, 147–181. [CrossRef]
33. Isselin, J.C.; Alloncle, A.P.; Autric, M. On laser induced single bubble near a solid boundary: Contribution to the understanding of erosion phenomena. *J. Appl. Phys.* **1998**, *84*, 5766–5771. [CrossRef]

34. Shaw, S.J.; Schiffers, W.P.; Gentry, T.P.; Emmony, D.C. The interaction of a laser-generated cavity with a solid boundary. *J. Acoust. Soc. Am.* **2000**, *107*, 3065–3072. [CrossRef]
35. Zhang, Y.L.; Yeo, K.S.; Khoo, B.C.; Wang, C. 3D Jet Impact and Toroidal Bubbles. *J. Comput. Phys.* **2001**, *166*, 336–360. [CrossRef]
36. Johnsen, E.; Colonius, T. Numerical simulations of non-spherical bubble collapse. *J. Fluid Mech.* **2009**, *629*, 231–262. [CrossRef] [PubMed]
37. Ochiai, N.; Iga, Y.; Nohmi, M.; Ikohagi, T. Numerical Analysis of Nonspherical Bubble Collapse Behavior and Induced Impulsive Pressure during First and Second Collapses near the Wall Boundary. *J. Fluid Sci. Technol.* **2011**, *6*, 860–874. [CrossRef]
38. Lauer, E.; Hu, X.; Hickel, S.; Adams, N. Numerical modelling and investigation of symmetric and asymmetric cavitation bubble dynamics. *Comput. Fluids* **2012**, *69*, 1–19. [CrossRef]
39. Chahine, G.L. Modeling of Cavitation Dynamics and Interaction with Material. In *Advanced Experimental and Numerical Techniques for Cavitation Erosion Prediction. Fluid Mechanics and Its Applications*; Kim, K.H., Chahine, G., Franc, J.P., Karimi, A., Eds.; Springer: Dordrecht, The Netherlands, 2014; Volume 106, pp. 123–161. [CrossRef]
40. Hsiao, C.T.; Jayaprakash, A.; Kapahi, A.; Choi, J.K.; Chahine, G.L. Modelling of material pitting from cavitation bubble collapse. *J. Fluid Mech.* **2014**, *755*, 142–175. [CrossRef]
41. Tiwari, A.; Pantano, C.; Freund, J. Growth-and-collapse dynamics of small bubble clusters near a wall. *J. Fluid Mech.* **2015**, *775*, 1–23. [CrossRef]
42. Koch, M.; Lechner, C.; Reuter, F.; Köhler, K.; Mettin, R.; Lauterborn, W. Numerical modeling of laser generated cavitation bubbles with the finite volume and volume of fluid method, using OpenFOAM. *Comput. Fluids* **2016**, *126*, 71–90. [CrossRef]
43. Aganin, A.A.; Ilgamov, M.A.; Kosolapova, L.A.; Malakhov, V.G. Dynamics of a cavitation bubble near a solid wall. *Thermophys. Aeromech.* **2016**, *23*, 211–220. [CrossRef]
44. Reuter, F.; Gonzalez-Avila, S.R.; Mettin, R.; Ohl, C.D. Flow fields and vortex dynamics of bubbles collapsing near a solid boundary. *Phys. Rev. Fluids* **2017**, *2*, 064202. [CrossRef]
45. Lechner, C.; Koch, M.; Lauterborn, W.; Mettin, R. Pressure and tension waves from bubble collapse near a solid boundary: A numerical approach. *J. Acoust. Soc. Am.* **2017**, *142*, 3649–3659. [CrossRef] [PubMed]
46. Zhang, S.; Zhang, A.M.; Wang, S.P.; Cui, J. Dynamic characteristics of large scale spark bubbles close to different boundaries. *Phys. Fluids* **2017**, *29*, 092107. [CrossRef]
47. Ma, X.; Huang, B.; Li, Y.; Chang, Q.; Qiu, S.; Su, Z.; Fu, X.; Wang, G. Numerical simulation of single bubble dynamics under acoustic travelling waves. *Ultrason. Sonochem.* **2018**, *42*, 619–630. [CrossRef] [PubMed]
48. Beig, S.A.; Aboulhasanzadeh, B.; Johnsen, E. Temperatures produced by inertally collapsing bubbles near rigid surfaces. *J. Fluid Mech.* **2018**, *852*, 105–125. [CrossRef]
49. Lauterborn, W.; Lechner, C.; Koch, M.; Mettin, R. Bubble models and real bubbles: Rayleigh and energy-deposit cases in a Tait-compressible liquid. *IMA J. Appl. Math.* **2018**, *83*, 556–589. [CrossRef]
50. Dular, M.; Požar, T.; Zevnik, J.; Petkovšek, R. High speed observation of damage created by a collapse of a single cavitation bubble. *Wear* **2019**, *418–419*, 13–23. [CrossRef]
51. Sagar, H.J.; el Moctar, O. Dynamics of a cavitation bubble near a solid surface and the induced damage. *J. Fluids Struct.* **2020**, *92*, 102799. [CrossRef]
52. Denner, F.; Evrard, F.; van Wachem, B. Modeling acoustic cavitation using a pressure-based algorithm for polytropic fluids. *Fluids* **2020**, *5*, 69. [CrossRef]
53. Lechner, C.; Lauterborn, W.; Koch, M.; Mettin, R. Jet formation from bubbles near a solid boundary in a compressible liquid: Numerical study of distance dependence. *Phys. Rev. Fluids* **2020**, *5*, 093604. [CrossRef]
54. Gonzalez-Avila, S.; Denner, F.; Ohl, C.D. The acoustic pressure generated by the cavitation bubble expansion and collapse near a rigid wall. *Phys. Fluids* **2021**, *33*, 032118. doi: 10.1063/5.0043822. [CrossRef]
55. Trummler, T.; Schmidt, S.J.; Adams, N.A. Effect of stand-off distance and spatial resolution on the pressure impact of near-wall vapor bubble collapses. *Int. J. Multiph. Flow* **2021**, *141*, 103618. [CrossRef]
56. Trummler, T.; Schmidt, S.J.; Adams, N.A. Numerical investigation of non-condensable gas effect on vapor bubble collapse. *Phys. Fluids* **2021**, *33*, 096107. [CrossRef]
57. Požar, T.; Agrež, V.; Petkovšek, R. Laser-induced cavitation bubbles and shock waves in water near a concave surface. *Ultrason. Sonochem.* **2021**, *73*, 105456. [CrossRef]
58. Koch, M. Laser Cavitation Bubbles at Objects: Merging Numerical and Experimental Methods. Ph.D. Thesis, Georg-August-Universität Göttingen, Third Physical Institute, Göttingen, Germany, 2020.
59. Koch, M.; Rosselló, J.M.; Lechner, C.; Lauterborn, W.; Eisener, J.; Mettin, R. Theory-assisted optical ray tracing to extract cavitation-bubble shapes from experiment. *Exp. Fluids* **2021**, *62*, 60. [CrossRef]
60. Lechner, C.; Lauterborn, W.; Koch, M.; Mettin, R. Fast, thin jets from bubbles expanding and collapsing in extreme vicinity to a solid boundary: A numerical study. *Phys. Rev. Fluids* **2019**, *4*, 021601. [CrossRef]
61. Pishchalnikov, Y.A.; Behnke-Parks, W.M.; Schmidmayer, K.; Maeda, K.; Colonius, T.; Kenny, T.W.; Laser, D.J. High-speed video microscopy and numerical modeling of bubble dynamics near a surface of urinary stone. *J. Acoust. Soc. Am.* **2019**, *146*, 516–531. [CrossRef] [PubMed]
62. Voinov, O.V.; Voinov, V.V. On the process of collapse of a cavitation bubble near a wall and the formation of a cumulative jet. *Sov. Phys. Dokl.* **1976**, *21*, 133–135.

63. Olaf, J. Oberflächenreinigung mit Ultraschall (Cleaning of surfaces by the use of ultrasonics). *Acustica* **1957**, *7*, 253–263.
64. Gale, G.; Busnaina, A. Roles of cavitation and acoustic streaming in megasonic cleaning. *Part. Sci. Technol.* **1999,** *17*, 229–238. [CrossRef]
65. Okorn-Schmidt, H.F.; Holsteyns, F.; Lippert, A.; Mui, D.; Kawaguchi, M.; Lechner, C.; Frommhold, P.E.; Nowak, T.; Reuter, F.; Banchs Piqué, M.; et al. Particle Cleaning Technologies to Meet Advanced Semiconductor Device Process Requirements. *ECS J. Solid State Sci. Technol.* **2014**, *3*, N3069–N3080. [CrossRef]
66. Mason, T.J. Ultrasonic cleaning: An historical perspective. *Ultrason. Sonochem.* **2016**, *29*, 519–523. [CrossRef]
67. Vlachomitrou, M.; Pelekasis, N. Numerical study of the interaction between a pulsating coated bubble and a rigid wall. *Phys. Rev. Fluids* **2021**, *6*, 013602-1–013602-33. [CrossRef]
68. Ohl, C.D.; Arora, M.; Dijkink, R.; Janve, V.; Lohse, D. Surface cleaning from laser-induced cavitation bubbles. *Appl. Phys. Lett.* **2006**, *89*, 074102. [CrossRef]
69. Reuter, F.; Mettin, R. Mechanisms of single bubble cleaning. *Ultrason. Sonochem.* **2016**, *29*, 550–562. [CrossRef]
70. Reuter, F.; Lauterborn, S.; Mettin, R.; Lauterborn, W. Membrane cleaning with ultrasonically driven bubbles. *Ultrason. Sonochem.* **2017**, *37*, 542–560. [CrossRef]
71. Kim, T.H.; Kim, H.Y. Disruptive bubble behaviour leading to microstructure damage in an ultrasonic field. *J. Fluid Mech.* **2014**, *750*, 355–371. [CrossRef]
72. Kauer, M.; Belova-Magri, V.; Cairós, C.; Linka, G.; Mettin, R. High-speed imaging of ultrasound driven Cavitation bubbles in blind and through holes. *Ultrason. Sonochem.* **2018**, *48*, 39–50. [CrossRef] [PubMed]
73. Karri, B.; Pillai, K.S.; Klaseboer, E.; Ohl, S.W.; Khoo, B.C. Collapsing bubble induced pumping in a viscous fluid. *Sens. Actuators A Phys.* **2011**, *169*, 151–163. [CrossRef]
74. Trummler, T.; Bryngelson, S.H.; Schmidmayer, K.; Schmidt, S.J.; Colonius, T.; Adams, N.A. Near-surface dynamics of a gas bubble collapsing above a crevice. *J. Fluid Mech.* **2020**, *899*, A16. [CrossRef]
75. Andrews, E.D.; Rivas, D.F.; Peters, I.R. Cavity collapse near slot geometries. *J. Fluid Mech.* **2020**, *901*, A29. [CrossRef]
76. Quah, E.W.; Karri, B.; Ohl, S.W.; Klaseboer, E.; Khoo, B.C. Expansion and collapse of an initially off-centered bubble within a narrow gap and the effect of a free surface. *Int. J. Multiph. Flow* **2018**, *99*, 62–72. [CrossRef]
77. Gonzalez-Avila, S.R.; van Blokland, A.C.; Zheng, Q.; Ohl, C.D. Jetting and shear stress enhancement from cavitation bubbles collapsing in a narrow gap. *J. Fluid Mech.* **2020**, *884*, A23-1–A32-23. [CrossRef]
78. Li, S.; Zhang, A.M.; Han, R.; Liu, Y.Q. Experimental and numerical study on bubble-sphere interaction near a rigid wall. *Phys. Fluids* **2017**, *29*, 092102. [CrossRef]
79. Zhang, Y.; Chen, F.; Zhang, Y.; Zhang, Y.; Du, X. Experimental investigations of interactions between a laser-induced cavitation bubble and a spherical particle. *Exp. Therm. Fluid Sci.* **2018**, *98*, 645–661. [CrossRef]
80. Li, S.; Zhang, A.M.; Han, R.; Ma, Q. 3D full coupling model for strong interaction between a pulsating bubble and a movable sphere. *J. Comput. Phys.* **2019**, *392*, 713–731. [CrossRef]
81. Zevnik, J.; Dular, M. Cavitation bubble interaction with a rigid spherical particle on a microscale. *Ultrason. Sonochem.* **2020**, *69*, 105252. [CrossRef]
82. Palanker, D.; Vankov, A.; Miller, J.; Friedman, M.; Strauss, M. Prevention of tissue damage by water jet during cavitation. *J. Appl. Phys.* **2003**, *94*, 2654–2661. [CrossRef]
83. Kim, D.; Kim, D. Underwater bubble collapse on a ridge-patterned structure. *Phys. Fluids* **2020**, *32*, 053312. [CrossRef]
84. Kadivar, E.; el Moctar, O.; Skoda, R.; Löschner, U. Experimental study of the control of cavitation-induced erosion created by collapse of single bubbles using a micro structured riblet. *Wear* **2021**, *486–487*, 204087. [CrossRef]
85. Zhang, Y.; Qiu, X.; Zhang, X.; Tang, N.; Zhang, Y. Collapsing dynamics of a laser-induced cavitation bubble near the edge of a rigid wall. *Ultrason. Sonochem.* **2020**, *67*, 105157. [CrossRef]
86. Senegačnik, M.; Kunimoto, K.; Yamaguchi, S.; Kimura, K.; Sakka, T.; Gregorčič, P. Dynamics of laser-induced cavitation bubble during expansion over sharp-edge geometry submerged in liquid – an inside view by diffuse illumination. *Ultrason. Sonochem.* **2021**, *73*, 105460. [CrossRef]
87. Wang, Q.; Mahmud, M.; Cui, J.; Smith, W.R.; Walmsley, A.D. Numerical investigation of bubble dynamics at a corner. *Phys. Fluids* **2020**, *32*, 053306. [CrossRef]
88. Koch, S.; Garen, W.; Hegedűs, F.; Neu, W.; Reuter, R.; Teubner, U. Time-resolved measurements of shock-induced cavitation bubbles in liquids. *Appl. Phys. B* **2012**, *108*, 345–351. [CrossRef]
89. Garen, W.; Hegedűs, F.; Kai, Y.; Koch, S.; Meyerer, B.; Neu, W.; Teubner, U. Shock wave emission during the collapse of cavitation bubbles. *Shock Waves* **2016**, *26*, 385–394. [CrossRef]
90. Fujikawa, S.; Akamatsu, T. Effects of the non-equilibrium condensation of vapour on the pressure wave produced by the collapse of a bubble in a liquid. *J. Fluid Mech.* **1980**, *97*, 481–512. [CrossRef]
91. Akhatov, I.; Lindau, O.; Topolnikov, A.; Mettin, R.; Vakhitova, N.; Lauterborn, W. Collapse and rebound of a laser-induced cavitation bubble. *Phys. Fluids* **2001**, *13*, 2805–2819. [CrossRef]
92. Akhatov, I.; Vakhitova, N.; Topolnikov, A.; Zakirov, K.; Wolfrum, B.; Kurz, T.; Lindau, O.; Mettin, R.; Lauterborn, W. Dynamics of laser-induced cavitation bubbles. *Exp. Therm. Fluid Sci.* **2002**, *26*, 731–737. [CrossRef]
93. Gopala, V.R.; van Wachem, B.G.M. Volume of fluid methods for immiscible-fluid and free-surface flows. *Chem. Eng. J.* **2008**, *141*, 204–221. [CrossRef]

94. Miller, S.; Jasak, H.; Boger, D.; Paterson, E.; Nedungadi, A. A pressure-based, compressible, two-phase flow finite volume method for underwater explosions. *Comput. Fluids* **2013**, *87*, 132–143. [CrossRef]
95. Hentschel, W.; Lauterborn, W. Acoustic emission of single laser-produced cavitation bubbles and their dynamics. *Appl. Sci. Res.* **1982**, *38*, 225–230. [CrossRef]
96. Brujan, E.A.; Nahen, K.; Schmidt, P.; Vogel, A. Dynamics of laser-induced cavitation bubbles near elastic boundaries: influence of the elastic modulus. *J. Fluid Mech.* **2001**, *433*, 283–314. [CrossRef]
97. Reuter, F.; Kaiser, S.A. High-speed film-thickness measurements between a collapsing cavitation bubble and a solid surface with total internal reflection shadowmetry. *Phys. Fluids* **2019**, *31*, 097108. [CrossRef]
98. Lauterborn, W. Cavitation bubble dynamics—New tools for an intricate problem. *Appl. Sci. Res.* **1982**, *38*, 165–178. [CrossRef]
99. Zhang, D.; Gökce, B.; Barcikowski, S. Laser synthesis and processing of colloids: fundamentals and applications. *Chem. Rev.* **2017**, *117*, 3990–4103. [CrossRef] [PubMed]